The Astrophysical Journal, 843:20 (31pp), 2017 July 1 https://doi.org/10.3847/1538-4357/aa7678

Planetary Nebulae and H II Regions in the Starburst Irregular Galaxy NGC 4449 from LBT MODS Data

F. Annibali[1], M. Tosi[1], D. Romano[1], A. Buzzoni[1], F. Cusano[1], M. Fumana[2], A. Marchetti[2], M. Mignoli[1], A. Pasquali[3], and A. Aloisi[4]
[1] INAF-Osservatorio Astronomico di Bologna, Via Gobetti 93/3, I-40129 Bologna, Italy; francesca.annibali@oabo.inaf.it
[2] INAF-Istituto di Astrofisica Spaziale e Fisica Cosmica, Via Bassini 15, I-20133 Milano, Italy
[3] Astronomisches Rechen-Institut, Zentrum fuer Astronomie der Universitaet Heidelberg, Moenchhofstr. 12-14, D-69120 Heidelberg, Germany
[4] Space Telescope Science Institute, 3700 San Martin Drive, Baltimore, MD 21218, USA
Received 2016 November 9; revised 2017 May 12; accepted 2017 May 25; published 2017 June 27

Abstract

We present deep 3500–10000 Å spectra of H II regions and planetary nebulae (PNe) in the starburst irregular galaxy NGC 4449, acquired with the Multi Object Double Spectrograph at the Large Binocular Telescope. Using the "direct" method, we derived the abundance of He, N, O, Ne, Ar, and S in six H II regions and in four PNe in NGC 4449. This is the first case of PNe studied in a starburst irregular outside the Local Group. Our H II region and PN sample extends over a galactocentric distance range of ≈2 kpc and spans ≈0.2 dex in oxygen abundance, with average values of $12 + \log(\mathrm{O/H}) = 8.37 \pm 0.05$ and 8.3 ± 0.1 for H II regions and PNe, respectively. PNe and H II regions exhibit similar oxygen abundances in the galactocentric distance range of overlap, while PNe appear more than ∼1 dex enhanced in nitrogen with respect to H II regions. The latter result is the natural consequence of N being mostly synthesized in intermediate-mass stars and brought to the stellar surface during dredge-up episodes. On the other hand, the similarity in O abundance between H II regions and PNe suggests that NGC 4449's interstellar medium has been poorly enriched in α-elements since the progenitors of the PNe were formed. Finally, our data reveal the presence of a negative oxygen gradient for both H II regions and PNe, while nitrogen does not exhibit any significant radial trend. We ascribe the (unexpected) nitrogen behavior to local N enrichment by the conspicuous Wolf-Rayet population in NGC 4449.

Key words: galaxies: abundances – galaxies: dwarf – galaxies: individual (NGC 4449) – galaxies: starburst – H II regions – planetary nebulae: general

1. Introduction

Stellar evolution and galaxy evolution are closely coupled: on the one hand, subsequent generations of high- and intermediate-mass stars continuously modify the energy balance and chemical composition of the interstellar medium (ISM) of their host galaxy; on the other hand, gas accretion by diffuse or filamentary cold streams (Dekel et al. 2009) or by gas-rich dwarfs may trigger new star formation and dilute the metallicity of the ISM. It is thus mandatory to combine accurate star formation histories (SFHs) from resolved stellar studies and chemical abundance studies in individual systems as key ingredients to reconstruct a coherent and complete picture of how galaxies formed and evolved.

Since the advent of the *Hubble Space Telescope* (*HST*), much effort has been made to resolve the individual stars and to derive the SFHs in large galaxy samples within the local Universe (e.g., Dalcanton et al. 2009, 2012; McQuinn et al. 2010; Monelli et al. 2010a, 2010b; Weisz et al. 2011, 2014; Calzetti et al. 2015, see also Tolstoy et al. 2009, for a review). At the same time, the availability of multiobject spectroscopy on 8–10 m telescopes has promoted chemical composition studies of H II regions and planetary nebulae (PNe) over large galaxy areas (e.g., Bresolin et al. 2005, 2009b; Magrini et al. 2005; Peña et al. 2007; Magrini & Gonçalves 2009; Stasińska et al. 2013; Annibali et al. 2015; Berg et al. 2015). In particular, the simultaneous study of chemical abundances in PNe and in H II regions can provide more stringent constraints on chemical evolution models, since H II regions probe the present-day composition of the ISM, while PNe, being the end product of the evolution of stars with masses $0.8\,M_{\odot} < M < 8\,M_{\odot}$, offer a view of the ISM composition back to several gigayears ago.

PNe enrich the ISM mainly in He, C and N, while leaving untouched elements such as Ne, S, and Ar whose abundance remains the initial one of the PN progenitor. O is also usually thought to be unaffected by the progenitor reaction processes, although it has sometimes been suggested to be enhanced (Marigo 2001) in metal-poor PNe. The important production of He, C, and N by PNe is due to dredge-up episodes occurring during the red giant branch (RGB) and asymptotic giant branch (AGB) phases of intermediate- and low-mass stars and to hot-bottom burning (HBB; e.g., Renzini & Voli 1981) in the most massive AGB stars ($\gtrsim 4\,M_{\odot}$, depending on metallicity), which change the stellar surface abundances of these elements.

Here we exploited the high performance of the Multi Object Double Spectrograph (MODS) mounted on the Large Binocular Telescope (LBT) to perform the first combined study of H II regions and PNe in the irregular galaxy NGC 4449 ($\alpha_{2000} = 12^{\mathrm{h}}28^{\mathrm{m}}11\overset{\mathrm{s}}{.}9$, $\delta_{2000} = +44°05'40''$), at a distance of 3.82 ± 0.27 Mpc from us (Annibali et al. 2008). NGC 4449 is of particular interest because it is one of the strongest starbursts in the local universe (star formation rate of $\sim 1\,M_{\odot}\,\mathrm{yr}^{-1}$, or $\sim 0.04\,M_{\odot}\,\mathrm{yr}^{-1}\,\mathrm{kpc}^{-2}$; McQuinn et al. 2010; Annibali et al. 2011); moreover, it exhibits several characteristics suggesting that it has accreted one or possibly several smaller companions. More specifically, (i) it has a very extended H I halo (≈90 kpc in diameter), which is a factor of ∼10 larger than the optical diameter of the galaxy and rotates in the opposite direction to the gas in the center (Hunter et al. 1998); (ii) it is one of the very few dwarf

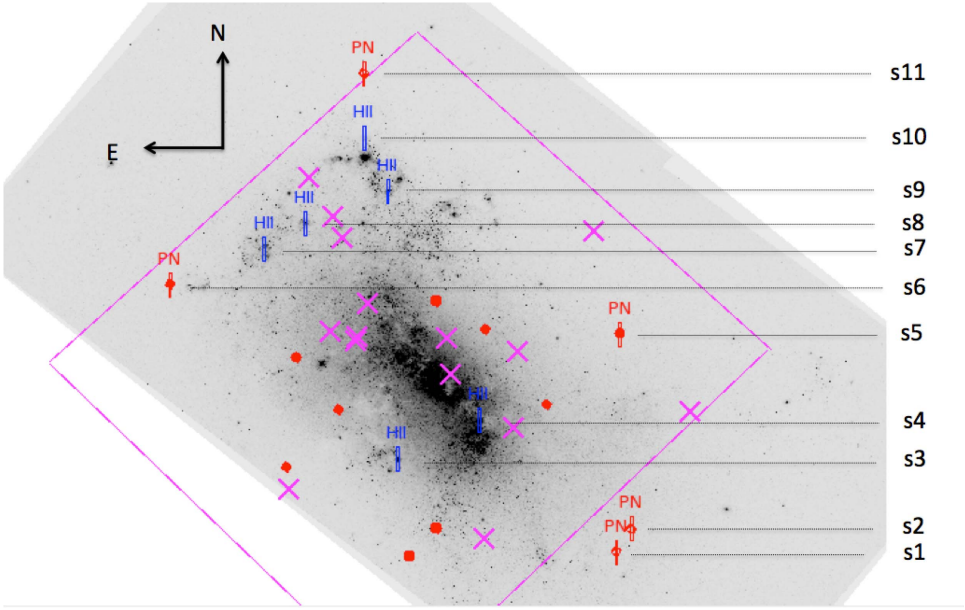

Figure 1. *HST*/ACS image of NGC 4449 in F555W ($\sim V$) with our H II region and PN sample superimposed. The smaller FOV covered by the ACS F502N ($\sim$[O III]) image is also indicated with the magenta line. The small red points and magenta crosses indicate the totality of the 28 PNe identified from the combined F435W ($\sim B$)–F502N–F814W (I) image and then cross-checked in F658N (Hα). The small red points denote the 13 PNe also identified when using the combined B, V, I image. Superimposed on the image are the 11 LBT/MODS $1'' \times 10''$ slits at the position of the six H II regions and five PNe targeted for spectroscopy.

galaxies where a stellar tidal stream has been discovered so far (Martínez-Delgado et al. 2012; Rich et al. 2012); (iii) it hosts an old, $10^6\,M_\odot$ cluster associated with two tails of young stars, potentially the nucleus of an accreted gas-rich satellite galaxy (Annibali et al. 2012). Because of these properties, NGC 4449 is a perfect laboratory to test the hypothesis that strong starbursts in dwarf galaxies are caused by accretion or merging events, as suggested by recent studies showing that disturbed H I kinematics, H I companions, and filamentary H I structures are more common in starburst dwarfs than in typical star-forming irregulars (Lelli et al. 2014). NGC 4449 was targeted with the Advanced Camera for Survey (ACS) on board *HST* a few years ago to resolve its stellar content and to derive its SFH (Annibali et al. 2008; McQuinn et al. 2010; Sacchi et al. 2017). These analyses indicate that NGC 4449 enhanced its SF activity $\approx$500 Myr ago, while the rate was much lower at earlier epochs; however, the impossibility of reaching, even with *HST*, the main-sequence turnoffs at a distance of $\sim$4 Mpc implies that the SFH of NGC 4449 is very uncertain prior to 1–2 Gyr ago (see, e.g., Sacchi et al. 2017).

In this paper we present a study of the H II region and PN chemical abundances in NGC 4449 with the purpose of providing a key complement to previous stellar population studies. Chemical evolution models based on the SFH and on the derived abundances (see, e.g., the approach of Romano et al. 2006) will be presented in a forthcoming paper and will provide new insights into the past evolution of NGC 4449. The paper is structured as follows: Section 2 describes the observations and data reduction, Section 3 provides information on the procedure for the derivation of the reddening-corrected emission-line fluxes, while temperatures, densities, and chemical abundances of H II regions and PNe are derived in Section 4. Section 5 focuses on the study of the Wolf-Rayet (W-R) spectral features. In Sections 6 and 7 we analyze and discuss the derived abundances, element ratios, and spatial abundance distributions, while in Section 8 we compare the properties of our PNe with those of Local Group star-forming dwarfs. Our conclusions are summarized in Section 9.

2. Observations and Data Reduction

PN candidates and H II regions were identified on *HST*/ACS images in the F435W ($\sim B$), F555W ($\sim V$), F814W ($\sim I$), and F658N (Hα) filters (GO program 10585; PI: Aloisi). These data cover a field of view (FOV) as large as $\sim 400'' \times 200''$ (two ACS pointings) and allow us to identify both H II regions and PNe up to large galactocentric distances. In the ACS images, H II regions are resolved and appear as regions of diffuse Hα and V (i.e., [O III]$\lambda\lambda$4959, 5007) emission. On the other hand, PN candidates were visually selected from a B, V, I color-combined image looking for point-like sources that stand out in V compared to B and I because of the [O III]$\lambda\lambda$4959, 5007 emission lines. The 29 selected candidates were then cross-identified on the shallower Hα image to eliminate background emission-line sources. This provided 13 PN candidates in NGC 4449, whose spatial location is shown in Figure 1. We repeated the PN search using archival ACS images in the narrowband F502N filter (GO program 10522; PI: Calzetti) instead of the F555W image and then cross-checked in Hα. The F502N filter, centered around the [O III] λ5007 line, allows for a better contrast of the PNe compared to stars; however, the smaller $\sim 200'' \times 200''$ FOV of the available data (corresponding to just one ACS pointing) does not permit an inspection of the NGC 4449 outskirts, where PNe can be more easily studied thanks to the lower galaxy background. All the PNe that were identified from the F555W image were also found when using the F502N image (however, three PNe fall outside the FOV of the F502N image); 15 additional PNe were identified when adopting the F502N image in place of the F555W one (see Figure 1), for a total sample of 28 PNe.

PNe and H II regions were targeted for spectroscopy with LBT/MODS from 2013 January 21, until 2013 April 5, within program 2012B_23, RUN A (PI Annibali). The $1'' \times 10''$ slit mask is shown in Figure 1. We were able to accomodate into the MODS slit mask 5 PNe out of 28, chosen in the most external regions of NGC 4449 to minimize the contamination from the diffuse ionized gas. Six remaining slits were positioned on H II regions.

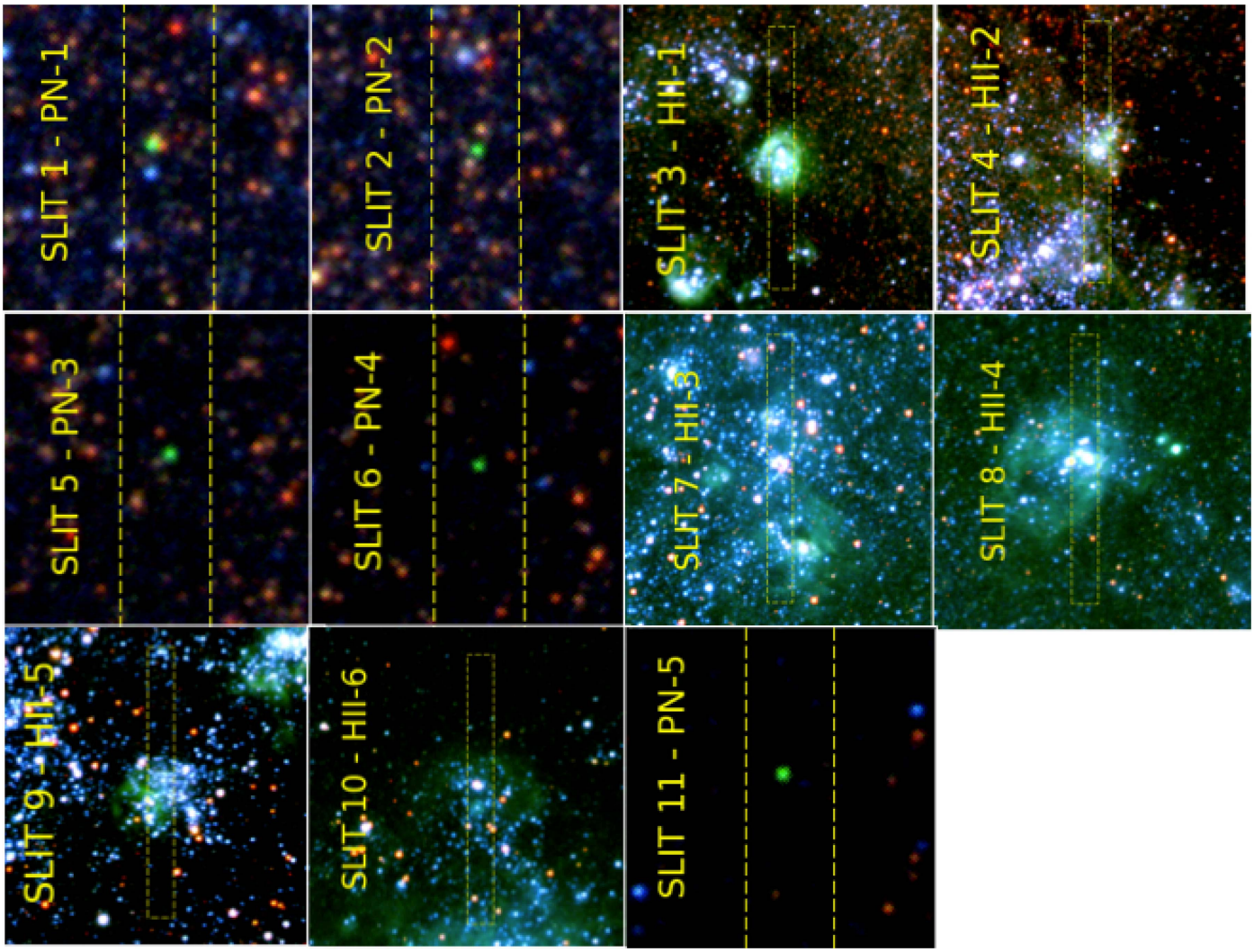

Figure 2. *HST*/ACS color-combined images (F435W = blue; F555W = green; F814W = red) of PNe and H II regions in NGC 4449 targeted for spectroscopy with LBT/MODS. The FOV shown is $\sim 3\farcs5 \times 3\farcs5$ for the PNe and $12'' \times 12''$ for the H II regions.

Table 1
Journal of LBT/MODS Observations

Exp. n.	Date-obs	Exptime	Avg. Seeing	Avg. Airmass	Retained?
1	2013 Jan 21	2700 s	$0\farcs6$	1.0	yes
2	2013 Jan 21	2700 s	$0\farcs6$	1.0	yes
3	2013 Jan 21	2700 s	$0\farcs7$	1.0	yes
4	2013 Apr 01	2700 s	$1\farcs0$	1.1	yes
5	2013 Apr 01	2700 s	$0\farcs8$	1.1	yes
6	2013 Apr 01	2700 s	$0\farcs7$	1.0	yes
7	2013 Apr 01	2700 s	$0\farcs8$	1.0	yes
8	2013 Apr 01	2700 s	$1\farcs1$	1.0	no
9	2013 Apr 01	2700 s	$1\farcs1$	1.1	no
10	2013 Apr 01	2700 s	$1\farcs1$	1.2	no
11	2013 Apr 01	3040 s	$2\farcs0$	1.3	no
12	2013 Apr 02	2700 s	$0\farcs9$	1.0	yes
13	2013 Apr 02	2700 s	$1\farcs3$	1.1	no
14	2013 Apr 05	2700 s	$1\farcs3$	1.0	no

Figure 2 shows color-composite *HST* images for the PNe and H II regions targeted with LBT, with the MODS slits superimposed. We observed our targets using the blue G400L (3200–5800 Å) and the red G670L (5000–10000 Å) gratings on the blue and red channels in dichroic mode for a total exposure time of ∼10.5 hr, organized into 14 subexposures of ∼2700 s each. The seeing varied between $\sim 0\farcs6$ and $\sim 1\farcs3$, and the airmass from ∼1.0 to ∼1.3. Typically, the exposures were acquired at hour angles between ∼−1 hr and ∼+1 hr to avoid significant effects from differential atmospheric refraction (see, e.g., Filippenko 1982). Only eight subexposures with a seeing $\lesssim 1''$ were retained for our study, for a total integration time of ∼6 hr. The journal of the observations is provided in Table 1.

Bias, flat-field, and wavelength calibrations were performed with the Italian LBT spectroscopic reduction facility at INAF-IASF Milano, producing the calibrated two-dimensional (2D) spectra for the individual subexposures. Then, the individual subexposures were sky-subtracted and combined into final 2D blue and red frames. The sky subtraction was performed with the *background* task in IRAF,[5] typically choosing the windows at the two opposite sides of the central source. This procedure removed, together with the sky, also the contribution from the NGC 4449 unresolved background. As an example, we show in Figure 3 the 2D sky-subtracted combined spectra for our PNe in selected spectral

[5] IRAF is distributed by the National Optical Astronomy Observatory, which is operated by the Association of Universities for Research in Astronomy, Inc., under cooperative agreement with the National Science Foundation.

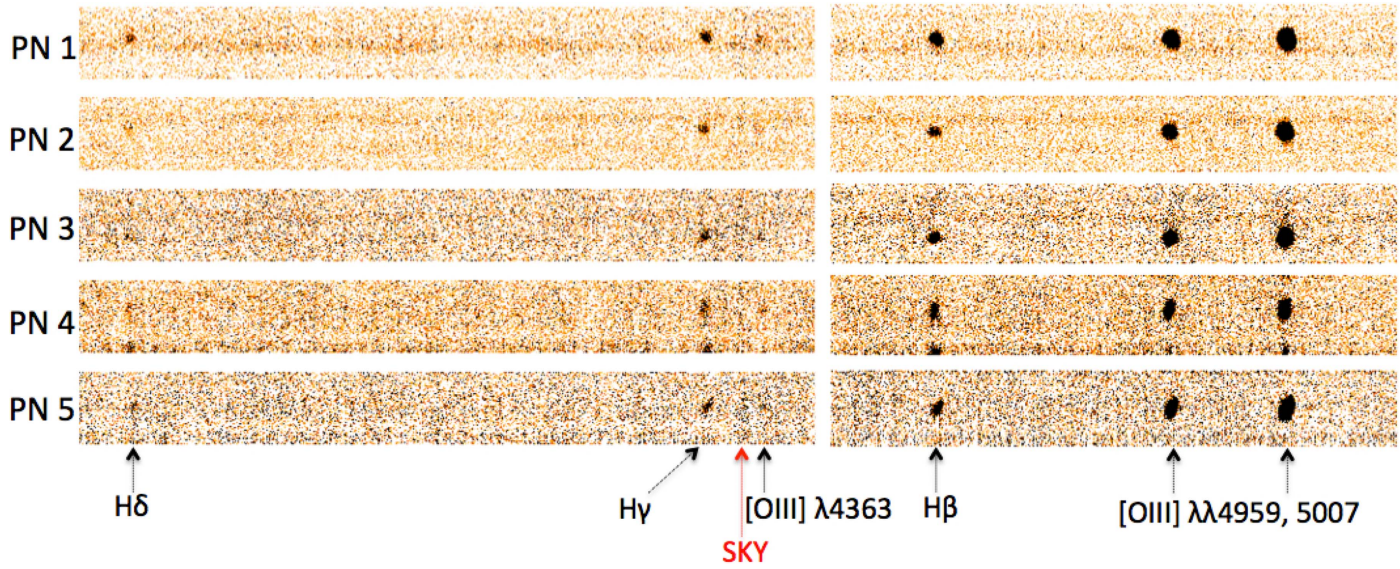

Figure 3. 2D MODS spectra of PNe in NGC 4449 showing the Hδ, Hγ, [O III]λ4363, Hβ, and [O III]$\lambda\lambda$4959, 5007 lines. The residuals corresponding to the subtraction of the Hg I λ4358 sky line, between the Hγ and [O III] λ4363 lines, are visible in the 2D spectra.

regions. The figure shows that we were able to detect the [O III] λ4363 line in all PNe thanks both to the good MODS resolution and to the NGC 4449's systemic velocity of $\approx$210 km s^{-1}, allowing for sufficient separation with the Hg I λ4358 sky line. For region H II-3, located in slit 7, it was not possible to evaluate the background, since the slit was entirely filled by gaseous emission. In this case, we adopted the background derived for PN 5 (slit 11) as a sky template and subtracted it from region H II-3. This is a reasonable choice because PN 5 is located at fairly large galactocentric distance and is affected by negligible contribution from the NGC 4449 unresolved background. The 1D spectra were extracted from the 2D calibrated and sky-subtracted spectra by running the *apall* task in the *twodspec* IRAF package. To derive the effective spectral resolution, we used the combined 1D spectra with no sky subtraction and measured the FWHM of the most prominent sky lines; this resulted in FWHM $\approx$ 4.1 Å (or $R \sim 1100$ at 4500 Å) for the blue channel and FWHM $\approx$ 5.8 Å (or $R \sim 1400$ at 8000 Å) for the red channel.

The blue and red 1D spectra were flux-calibrated using the sensitivity curves from the Italian LBT spectroscopic reduction pipeline; the curves were derived using the spectrophotometric standard star Feige 56 observed in dichroic mode with a 5″-width slit on 2013 April 1, at an airmass of $\sim$1.4. To obtain the red and blue sensitivity curves, the observed standard was compared with reference spectra in the *HST* CALSPEC database. Atmospheric extinction corrections were applied using the average extinction curve available from the MODS calibration webpage at http://www.astronomy.ohio-state.edu/MODS/Calib/. This may introduce some uncertainty in flux calibration, in particular at the bluest wavelengths, where the effect of atmospheric extinction is more severe. By comparing the sensitivity curves from Feige 56 with those obtained from another standard, Feige 66, observed on 2013 January 20, at an airmass of $\sim$1 and with the same setup of Feige 56 as part of our 2012B_23, RUN B program,[6] we found a $\sim$15% difference at wavelegnths below $\sim$4000 Å, while the curves agree within $\sim$1% at redder wavelengths.

Eventually, to evaluate the accuracy of the flux calibration for our spectra, we used *HST*/ACS imaging in F435W, F555W, F814W, and F658N from our GO program 10585 and archive *HST*/ACS imaging in F502N and F550M from GO program 10522 (PI Calzetti), with a smaller FOV. The six H II regions, plus PN-3 and PN-4, fall within the FOV of all six images; however, we considered only H II regions for the purpose of checking the flux calibration, because of their higher signal-to-noise ratio compared to PNe. Aperture photometry was performed on the images within the same extraction aperture of the 1D spetcra using the *Polyphot* task in IRAF. The F555W magnitudes in the ACS Vega mag system derived for the H II regions and the five PNe targeted with MODS are given in Tables 8 and 9 (see instead Table 7 in Section 8 for a complete list of the F555W and the F502N magnitudes derived for the total sample of 28 PNe). For the H II regions, we also computed synthetic magnitudes in the F435W, F502N, F550M, F555W, F814W, and F658N ACS filters by convolving the MODS spectra with the ACS bandpasses: this was done by running the *Calcphot* task in the *Synphot* package. Figure 4 shows, for each H II region, the comparison between the observed ACS fluxes and the synthetic ones (in logarithmic scale) as a function of wavelength. We notice that the $F_{\lambda,\mathrm{ACS}}$ fluxes are smaller than the $F_{\lambda,\mathrm{SYN}}$ ones, indicating that the fluxes from the spectra are overestimated. This effect is expected, and its origin is well discussed by Smith et al. (2007): flux calibrations are usually tied to reference point-source observations and therefore include an implicit correction for the fraction of the point-source light that falls outside the slit; however, in the limit of a perfect uniform, slit-filling extended source, the diffractive losses out of the slit are perfectly balanced by the diffractive gains into the slit from emission beyond its geometric boundary. Therefore, the point-source-based calibration will inevitably cause an overestimate of the extended source flux. The $\log(F_{\lambda,\mathrm{ACS}}) - \log(F_{\lambda,\mathrm{SYN}})$ zero-point offsets of Figure 4 were used to anchor our H II region spectra to the ACS magnitudes; this procedure is useful for establishing an absolute flux calibration for these objects. On

[6] During RUN B we targeted old unresolved stellar clusters in NGC 4449; the results will be presented in another paper (F. Annibali et al. 2017, in preparation).

Table 2
Reddening-corrected Emission Fluxes for H II Regions in NGC 4449

Line	H II-1	H II-2	H II-3	H II-4	H II-5	H II-6
[O II] λ3727	110 ± 20	190 ± 30	400 ± 70	250 ± 50	240 ± 40	480 ± 90
H10 λ3978	6 ± 1	6 ± 1	6 ± 1	7 ± 1	6 ± 1	6 ± 1
He I λ3820	0.9 ± 0.1	0.7 ± 0.1	⋯	0.6 ± 0.1	⋯	⋯
H9+He II λ3835	9 ± 1	8 ± 1	9 ± 1	9 ± 2	8 ± 1	9 ± 2
[Ne III] λ3869	32 ± 5	23 ± 4	14 ± 2	23 ± 4	18 ± 3	35 ± 6
H8+He I λ3889	19 ± 3	21 ± 4	20 ± 3	22 ± 4	21 ± 4	21 ± 4
Hϵ + He I +[Ne III] λ3970	25 ± 4	23 ± 4	21 ± 3	27 ± 5	24 ± 4	29 ± 5
He I λ4026	2.02 ± 0.06	1.8 ± 0.2	0.9 ± 0.1	1.5 ± 0.2	1.0 ± 0.1	⋯
[S II] λ4068	0.73 ± 0.03	0.77 ± 0.07	2.5 ± 0.2	1.0 ± 0.1	1.3 ± 0.2	3.9 ± 0.5
[S II] λ4076	0.21 ± 0.03	0.40 ± 0.04	0.79 ± 0.06	⋯	⋯	1.5 ± 0.2
Hδ λ4101	26.3 ± 0.8	29 ± 3	30 ± 2	33 ± 5	30 ± 4	30 ± 4
Hγ λ4340	46 ± 1	49 ± 4	50 ± 4	50 ± 7	50 ± 6	52 ± 6
[O III] λ4363	2.1 ± 0.1	1.8 ± 0.2	1.4 ± 0.1	1.6 ± 0.2	1.9 ± 0.2	2.4 ± 0.3
He I λ4389	0.57 ± 0.02	0.38 ± 0.03	⋯	0.48 ± 0.07	⋯	⋯
He I λ4471	4.6 ± 0.1	4.8 ± 0.4	4.1 ± 0.3	4.5 ± 0.6	4.2 ± 0.4	4.2 ± 0.4
N III(WR) λ4640	0.19 ± 0.01	⋯	⋯	1.1 ± 0.2	⋯	⋯
[C III](WR) λ4652	0.11 ± 0.03	⋯	⋯	0.5 ± 0.1	⋯	⋯
[Fe III] λ4658	0.14 ± 0.02	0.28 ± 0.02	0.84 ± 0.06	0.43 ± 0.07	0.50 ± 0.06	1.4 ± 0.2
He II (WR) λ4686	3.6 ± 0.2	⋯	⋯	6 ± 1	⋯	⋯
He II λ4686	0.4 ± 0.3	⋯	⋯	⋯	⋯	0.8 ± 0.1
[Ar IV]+He I λ4713	0.50 ± 0.05	0.38 ± 0.03	⋯	0.5 ± 0.1	⋯	⋯
[Ar IV] λ4740	0.16 ± 0.01	⋯	⋯	0.30 ± 0.06	⋯	⋯
Hβ λ4861	100 ± 3	100 ± 8	100 ± 7	100 ± 14	100 ± 11	100 ± 11
He I λ4922	1.20 ± 0.04	1.2 ± 0.1	0.76 ± 0.06	1.0 ± 0.2	0.8 ± 0.1	⋯
[O III] λ4959	143 ± 4	129 ± 11	71 ± 5	100 ± 20	110 ± 10	100 ± 10
[Fe III] λ4986	0.19 ± 0.02	0.37 ± 0.06	1.16 ± 0.09	0.38 ± 0.05	0.57 ± 0.07	1.9 ± 0.2
[O III] λ5007	420 ± 10	380 ± 30	210 ± 10	300 ± 40	320 ± 40	300 ± 30
He I λ5015	2.46 ± 0.07	2.7 ± 0.2	2.2 ± 0.2	2.3 ± 0.3	2.2 ± 0.2	2.2 ± 0.3
[N I] λ5199	0.21 ± 0.01	0.13 ± 0.01	1.01 ± 0.08	0.26 ± 0.04	0.34 ± 0.04	2.2 ± 0.2
He I λ5876	11.8 ± 0.3	12 ± 1	10.8 ± 0.8	12 ± 2	12 ± 1	13 ± 1
[O I] λ6302	1.17 ± 0.04	0.64 ± 0.06	⋯	1.1 ± 0.2	1.7 ± 0.2	9.4 ± 1.1
[S III] λ6314	1.12 ± 0.03	1.3 ± 0.1	1.2 ± 0.1	1.2 ± 0.2	1.3 ± 0.2	1.6 ± 0.2
[O I] λ6365	0.37 ± 0.01	0.17 ± 0.02	2.0 ± 0.2	0.39 ± 0.06	0.61 ± 0.08	3.1 ± 0.4
[N II] λ6548	2.9 ± 0.1	4.2 ± 0.4	8.8 ± 0.9	5.3 ± 0.8	4.9 ± 0.6	12 ± 1
Hα λ6563	287 ± 8	300 ± 30	300 ± 30	310 ± 50	300 ± 40	310 ± 40
[N II] λ6584	8.0 ± 0.3	12 ± 1	25 ± 2	16 ± 2	14 ± 2	35 ± 4
He I λ6678	3.5 ± 0.1	3.4 ± 0.3	3.4 ± 0.3	3.7 ± 0.6	3.4 ± 0.4	3.8 ± 0.5
[S II] λ6716	8.2 ± 0.2	7.1 ± 0.7	33 ± 3	15 ± 2	16 ± 2	51 ± 6
[S II] λ6731	6.0 ± 0.2	5.6 ± 0.5	24 ± 2	11 ± 2	12 ± 1	37 ± 5
He I λ7065	1.9 ± 0.1	2.1 ± 0.2	1.9 ± 0.2	2.1 ± 0.3	1.9 ± 0.2	1.8 ± 0.2
[Ar III] λ7136	8.4 ± 0.3	9.4 ± 0.9	7.1 ± 0.7	8 ± 1	9 ± 1	10 ± 1
He I λ7281	0.57 ± 0.02	0.59 ± 0.06	⋯	0.6 ± 0.1	0.63 ± 0.08	⋯
[O II] λ7320	1.14 ± 0.04	1.7 ± 0.2	⋯	2.2 ± 0.4	2.3 ± 0.3	4.1 ± 0.5
[O II] λ7330	0.96 ± 0.03	1.5 ± 0.1	⋯	1.8 ± 0.3	1.9 ± 0.2	3.3 ± 0.4
[Ar III] λ7751	2.25 ± 0.07	2.4 ± 0.2	⋯	1.9 ± 0.3	2.4 ± 0.3	2.0 ± 0.3
P10 λ9017	19.8 ± 0.5	15 ± 2	⋯	19 ± 3	20 ± 3	16 ± 2
[S III] λ9069	20.5 ± 0.7	21 ± 2	20 ± 2	21 ± 4	23 ± 3	22 ± 3
P9 λ9229	2.24 ± 0.08	2.1 ± 0.2	2.5 ± 0.3	2.4 ± 0.5	2.5 ± 0.4	⋯
[S III]λ9532	42 ± 1	51 ± 6	41 ± 5	44 ± 9	51 ± 8	46 ± 7
P8 λ9547	2.7 ± 0.1	3.1 ± 0.4	⋯	2.4 ± 0.5	2.6 ± 0.4	⋯
F(Hβ)[10^{-13} erg/s/cm^2]	0.35 ± 0.01	0.64 ± 0.08	0.41 ± 0.07	0.4 ± 0.1	0.21 ± 0.04	0.06 ± 0.01
$E(B-V)$	0.10 ± 0.01	0.24 ± 0.03	0.18 ± 0.05	0.20 ± 0.07	0.16 ± 0.05	0.23 ± 0.05

Note. Fluxes are given on a scale where $F(\mathrm{H}\beta) = 100$.

the other hand, no correction was applied to the PN spectra, for two main reasons: (1) these sources are point-like at NGC 4449's distance (also in the *HST* images), and therefore we do not expect the spectral fluxes to be overestimated as in the case of extended H II regions; and (2) synthetic fluxes derived by convolving the ACS filter throughputs with the PN spectra are highly affected by uncertainties in the background subtraction and do not permit a reliable comparison with the ACS photometry. The standard deviation around the average $\log F_{\lambda,\mathrm{ACS}} - \log F_{\lambda,\mathrm{SYN}}$ value derived for the H II regions is quite modest, corresponding to an average flux uncertainty in the range of ≈2%–≈11%. The low dispersion about the mean and the lack of a general trend with wavelength apparently confirm that our observational setup prevented significant flux

Table 3
Reddening-corrected Emission Fluxes for PNe in NGC 4449

Line	PN-1	PN-2	PN-3	PN-4	PN-5
[O II] λ3727	25 ± 7	80 ± 20	90 ± 20	400 ± 100	⋯
[Ne III] λ3869	70 ± 20	80 ± 20	70 ± 20	80 ± 20	90 ± 20
H8+He I λ3889	10 ± 3	23 ± 6	20 ± 5	24 ± 6	18 ± 5
Hϵ + He I +[Ne III] λ3970	30 ± 8	40 ± 10	40 ± 10	30 ± 9	⋯
Hδ λ4101	23 ± 5	31 ± 7	20 ± 5	⋯	⋯
Hγ λ4340	40 ± 8	60 ± 10	50 ± 10	60 ± 10	50 ± 10
[O III] λ4363	10 ± 3	20 ± 4	20 ± 4	20 ± 4	20 ± 4
He II λ4686	⋯	16 ± 3	40 ± 7	⋯	⋯
Hβ λ4861	100 ± 20	100 ± 20	100 ± 20	100 ± 20	100 ± 20
[O III] λ4959	390 ± 70	410 ± 70	400 ± 70	330 ± 60	430 ± 80
[O III] λ5007	1100 ± 200	1200 ± 200	1100 ± 200	900 ± 200	1200 ± 200
He I λ5876	11 ± 3	11 ± 3	7 ± 2	11 ± 2	14 ± 3
[N II] λ6548	10 ± 3	9 ± 3	24 ± 6	11 ± 3	5 ± 1
Hα λ6563	280 ± 70	280 ± 70	260 ± 70	280 ± 70	280 ± 70
[N II] λ6584	25 ± 7	36 ± 9	70 ± 20	24 ± 6	11 ± 3
[S II] λ6716	10 ± 3	11 ± 3	9 ± 2	27 ± 7	⋯
[S II] λ6731	11 ± 3	10 ± 3	11 ± 3	18 ± 5	⋯
He I λ7065	14 ± 4	⋯	⋯	⋯	7 ± 2
[Ar III] λ7136	8 ± 2	17 ± 5	9 ± 3	⋯	⋯
[S III] λ9069	18 ± 7	20 ± 10	19 ± 8	⋯	⋯
[S III] λ9532	30 ± 10	⋯	⋯	⋯	⋯
F(Hβ)[10^{-16}erg/s/cm^2]	0.52 ± 0.07	0.4 ± 0.3	0.35 ± 0.05	0.8 ± 0.5	0.4 ± 0.3
$E(B-V)$	0.0 ± 0.2	0.1 ± 0.2	0.0 ± 0.2	0.4 ± 0.2	0.1 ± 0.2

Note. Fluxes are given on a scale where $F(\mathrm{H}\beta) = 100$.

losses at the bluest wavelengths, possibly due to atmospheric differential refraction (Filippenko 1982).

As an example, we show the final calibrated spectra for H II region H II-1 and planetary nebula PN-1 in Figures 5 and 6, respectively. The spectra of all the other H II regions and PNe are provided in Figures 16–24 in Appendix A.

3. Emission-line Measurement

Emission-line fluxes for H II regions and PNe were obtained with the *deblend* function available in the *splot* IRAF task. We used this function to fit single lines, groups of lines close in wavelength, or blended lines. Lines were fitted with Gaussian profiles, treating the centroids and the widths as free parameters; however, when fitting groups of lines close in λ (e.g., He I λ6678 + [S II]λ6716 + [S II]λ6731) or (partially) blended (Hα + [N II]$\lambda\lambda$6548, 84), we forced the lines to have all the same width. On the other hand, no constraint on the line centroids (e.g., fixed separation between the lines) was assumed, and we let the *deblend* function find the best-fit line centers independently. This was a reasonable choice given that even faint "key" lines, such as [O III]λ4363 and [N II]$\lambda\lambda$6548, 6584, are detected with a good signal-to-noise ratio in our spectra; however, had we had worse data, it would have been more appropriate to set the wavelengths of the blended lines and to allow for a common Doppler shift, in order to reduce the noise on the weak-line measurement. The continuum was defined choosing two continuum windows to the left and to the right of the line or line complex and fitting with a linear regression. Balmer lines, potentially affected by underlying stellar absorption, were fitted with a combination of Voigt profiles in absorption plus Gaussian profiles in emission (see Section 3.1 for more details).

The final emission fluxes were obtained by repeating the measurement several times with slightly different continuum choices and averaging the results. To compute the errors, we derived the standard deviation of the different measurements ($\sigma_{F,\mathrm{line}}$). The results for the H II regions and the PNe are provided in Tables 8 and 9, respectively. From the tables, we notice that the errors on the derived fluxes are very small: for instance, in the case of H II regions, $\sigma_{F,\mathrm{line}}$ is below 1% for the brightest lines such as [O III]λ5007. To get more realistic errors, we added in quadrature to $\sigma_{F,\mathrm{line}}$ a 15% flux error below ∼4000 Å to account for atmospheric extinction uncertainties (see Section 2) and a 2% to 11% flux error, corresponding to the scatter around the average offsets in Figure 4, at redder wavelengths. For PNe, the standard deviation from the different line measurements turned out to be significantly larger than for H II regions, typically in the range of ≈2% to ≈20%; an arbitrary additional 15% error, equaling the flux calibration uncertainty below ∼4000 Å and slightly above the largest scatter for the H II regions in Figure 4, was added in quadrature to $\sigma_{F,\mathrm{line}}$ over the entire wavelength range.

3.1. Absorption from Underlying Stellar Population

To account for underlying stellar absorption in H II regions, spectral regions around Balmer lines were fitted with a combination of Voigt profiles (in absorption) and Gaussian profiles (in emission), as shown in Figure 7. Absorption wings are more prominent for bluer lines, because Balmer emission decreases very rapidly toward bluer wavelength, while the absorption equivalent widths remain roughly constant with wavelength. This implies that the contribution from absorption and emission can be better separated for bluer lines, while fits to red Balmer lines (Hβ and Hα) tend to be highly affected by a degeneracy between absorption strength and FWHM of the line. To overcome this problem, we fitted the H10(λ3798) and H9(λ3835) lines in the first place and then adopted the derived (Lorentian and Gaussian) FWHM values for the fits to all the

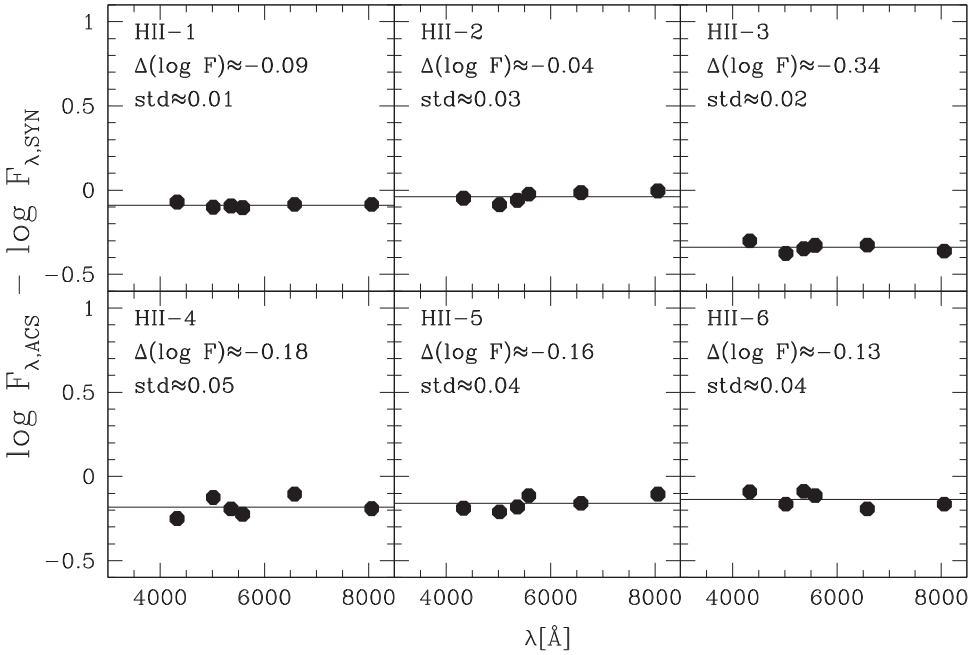

Figure 4. Comparison between ACS and *Synphot* fluxes for H II regions in NGC 4449 (see Section 2). From blue to red wavelengths, the filled circles correspond to the following ACS bandpasses: F435W, F502N, F555W, F550M, F658N, and F814W. For each H II region, the solid horizontal line is the average $\log(F_{\lambda,\mathrm{ACS}}) - \log(F_{\lambda,\mathrm{SYN}})$ offset. The standard deviation around this value is also indicated within each panel.

other Balmer lines up to Hβ. We derived average absorption equivalent widths and standard deviations of 3.3 ± 0.6 Å, 4.2 ± 0.7 Å, 4.2 ± 0.3 Å, 4.2 ± 0.6 Å, 4.9 ± 0.1 Å, 5.6 ± 0.3 Å, and 5.6 ± 1.2 Å for H10, H9, H8, Hϵ, Hδ, Hγ, and Hβ, respectively, compatible with a simple stellar population (SSP) of age $\simeq$10–20 Myr and $Z = 0.008$ (about NGC 4449's metallicity) from the Starburst99 models (Leitherer et al. 2014, hereafter SB99). For such an SSP, the models predict a typical absorption equivalent width of $\simeq$3.5 Å for Hα, to be compared with emission strengths in the range 100–2000 Å. Therefore, we neglected the effect of underlying absorption on the Hα + [N II] $\lambda\lambda$6548, 84 emission complex. In conclusion, our procedure accounts for the presence of underlying Balmer absorptions by simultaneously fitting the emission and absorption components, so that no further correction needs to be applied to the hydrogen emission lines.

As for helium, absorption wings are too shallow to allow for a decomposition of absorption and emission through spectral fits. Thus, we used the predictions of simple stellar population models to correct for this effect. The SB 99 models provide for a $\simeq$10–20 Myr old population with $Z = 0.008$ typical absorption equivalent widths of $\simeq$0.5 Å, $\simeq$0.3 Å, and $\simeq$0.3 Å in the He I λ4471, He I λ5876, and He I λ6678 lines, respectively. These contributions are not negligible when compared with observed emissions in the range $\simeq$1–9 Å, $\simeq$9–55 Å, and $\simeq$3–23 Å in our sample. Therefore, we adopted the absorption EWs provided by SB 99 and corrected the He I emission lines according to the formula $F'(\mathrm{He\ I}) = F(\mathrm{He\ I}) + \mathrm{EW_{abs}(SB\ 99)} * F(\mathrm{CONT})$, where F(He I) and F'(He I) are the "raw" and the corrected fluxes, respectively, $\mathrm{EW_{abs}}$(SB 99) is the stellar absorption equivalent width from the SB 99 models, and F(CONT) is the flux in the continuum measured from the spectra.

3.2. Reddening Correction

For H II regions, the reddening was derived from the Hδ/Hα, Hγ/Hα, and Hβ/Hα ratios assuming the Cardelli et al. (1989) extinction law with $R_V = 3.05$, according to the formula

$$E(B-V) = \frac{\log_{10}[(\mathrm{FH}_{\lambda1}/\mathrm{FH}_{\lambda2})_o/(\mathrm{FH}_{\lambda1}/\mathrm{FH}_{\lambda2})_t]}{0.4 \times R_V \times [A_{\lambda2}/A_V - A_{\lambda1}/A_V]}, \quad (1)$$

where $\lambda1$ and $\lambda2$ are the wavelengths of the two Balmer lines, $(\mathrm{FH}_{\lambda1}/\mathrm{FH}_{\lambda2})_o$ and $(\mathrm{FH}_{\lambda1}/\mathrm{FH}_{\lambda2})_t$ are, respectively, the observed and theoretical Balmer emission line ratios, and the magnitude attenuation ratio A_λ/A_V is that from Cardelli's law. We adopted theoretical Balmer ratios of $(\mathrm{FH}_\delta/\mathrm{FH}_\alpha)_t = 0.090$, $(\mathrm{FH}_\gamma/\mathrm{FH}_\alpha)_t = 0.163$, and $(\mathrm{FH}_\beta/\mathrm{FH}_\alpha)_t = 0.350$ from Storey & Hummer (1995) for case B recombination assuming $T_e = 10{,}000$ K and $n_e = 100\,\mathrm{cm}^{-3}$, and $A_{\mathrm{H}\delta}/A_V \sim 1.45$, $A_{\mathrm{H}\gamma}/A_V \sim 1.36$, $A_{\mathrm{H}\beta}/A_V \sim 1.17$, and $A_{\mathrm{H}\alpha}/A_V \sim 0.81$ from Cardelli's extinction curve. For each Balmer line ratio, the error in $E(B-V)$ was obtained by propagating the emission flux errors into Equation (1). It can be easily verified from Equation (1), and from the A_λ/A_V values reported above that, for equal emission flux errors, the reddening uncertainty is higher when using Balmer line ratios with closer wavelength spacing, minimizing the $A_{\lambda2} - A_{\lambda1}$ difference: for instance, a $\sim$5% flux error provides an error $\sigma_{E(B-V)}$ in the range of $\sim$0.04–0.07 mag if the reddening is estimated from the Hδ/Hα, Hγ/Hα, and Hβ/Hα ratios (as in our case), while using, e.g., Hδ/Hγ implies $\sigma_{E(B-V)}$ as high as $\sim$0.28 mag.

For H II regions, the reddening was obtained by averaging the results from the Hδ/Hα, Hγ/Hα, and Hβ/Hα ratios, and its uncertainty was computed as the standard deviation; typically, the $E(B-V)$ values derived from the three different Balmer ratios turned out to be consistent with each other, within the errors. Differences in the $E(B-V)$ values obtained from different Balmer lines may arise from the fact that redder lines, affected by a lower extinction, probe larger optical depths of the nebula (Calzetti et al. 1996). For PNe, we used instead only the Hβ/Hα ratio, due to the faintness of the other Balmer

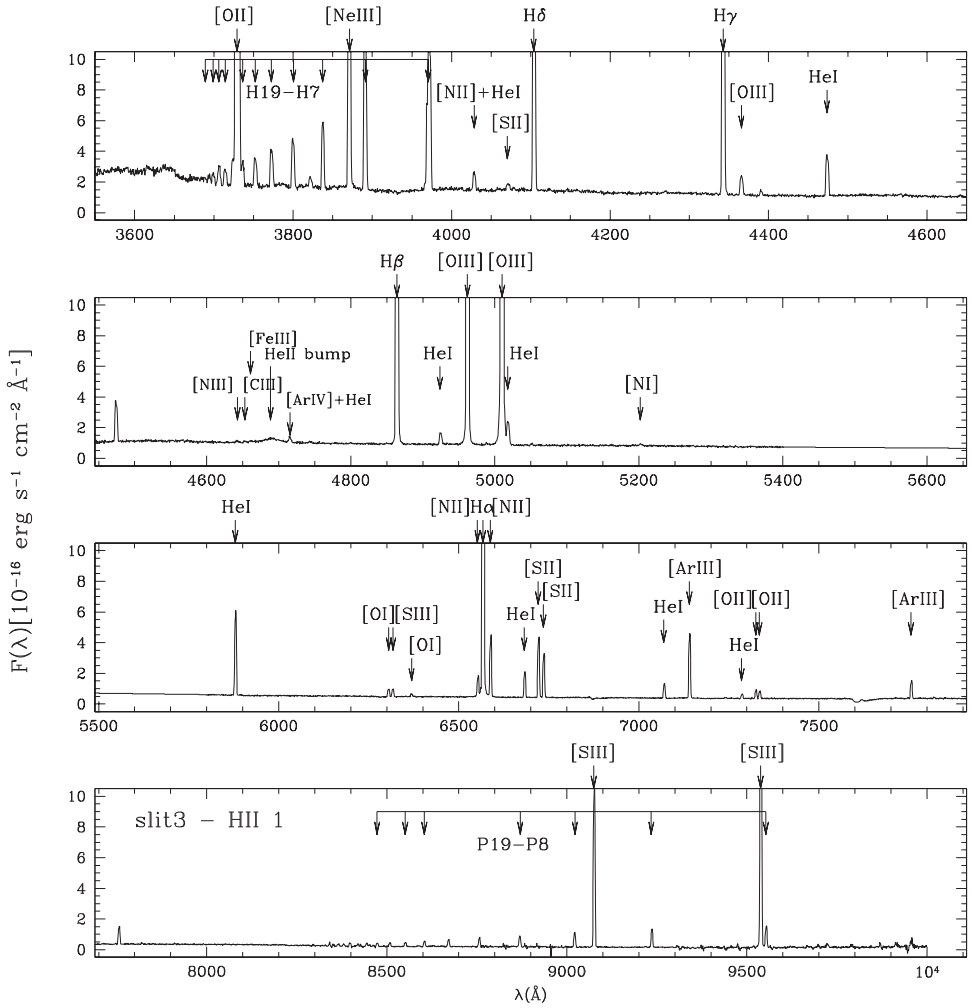

Figure 5. LBT/MODS spectra in the blue and red channels for H II-1 in NGC 4449 with all the identified emission lines indicated. A linear interpolation was performed in the 5400–5800 Å region, where the sensitivities of the blue and red detectors drop. The spectra of the other H II regions (H II-2, H II-3, H II-4, H II-5, H II-6) are provided in Appendix A.

lines. For H II regions, the derived $E(B-V)$ values are in the range of $\sim$0.10 $\pm$ 0.01 to 0.24 $\pm$ 0.03 mag, while for PNe they are in the range of $\approx$0–0.4 mag with a typical uncertainty of $\sim$0.2 mag.

The emission-line fluxes are corrected for reddening according to the formula

$$F_c = F_o \times 10^{0.4 \times A_\lambda}, \quad (2)$$

where F_o and F_c are the observed and the extinction-corrected fluxes, respectively, and $A_\lambda = (A_\lambda/A_V) \times R_V \times E(B-V)$. The derived $E(B-V)$ values and the reddening-corrected emission-line fluxes for H II regions and PNe are given in Tables 2 and 3, respectively.

4. Temperatures, Densities, and Chemical Abundances

Temperatures, densities, and chemical abundances for H II regions and PNe were derived using the *getCrossTemDen* and *getIonAbundance* options in the 1.0.1 version of the PyNeb code (Luridiana et al. 2015), which is based on the FIVEL program developed by De Robertis et al. (1987) and Shaw & Dufour (1994). The *getCrossTemDen* task simultaneously derives electron densities (n_e) and temperatures (T_e) through an iterative process assuming a density-sensitive and a temperature-sensitive diagnostic line ratio: the quantity (density or temperature) derived from one emission-line ratio is inserted into the other, and the process is iterated until the two temperature-sensitive and density-sensitive diagnostics give self-consistent results.

Once the physical conditions are known, the *getIonAbundance* task computes the ionic abundance of a given ion relative to H^+ from the observed emission-line intensities relative to Hβ. We ran PyNeb with the default data set for line emissivities, collision strengths, and radiative transition probabilities; the atomic data set sources for the various ions are provided in Table 4. Notice that the adopted emissivities for He^+ are those of Porter et al. (2012, 2013), which include collisional excitation.

4.1. H II Regions

For H II regions, n_e and T_e values were derived using the density-sensitive [S II] $\lambda6716/\lambda6731$ diagnostic line ratio and three sets of temperature-sensitive line ratios: [O III] $\lambda4363/\lambda4959 + \lambda5007$, [S III] $\lambda6312/\lambda9069 + \lambda9532$, and [O II] $\lambda7320 + \lambda7330/\lambda3726 + \lambda3729$. We found $n_e \lesssim 100\,\mathrm{cm}^{-3}$ and T_e in the range of 9000–11,000 K. Density and temperature values for the individual H II regions are given in

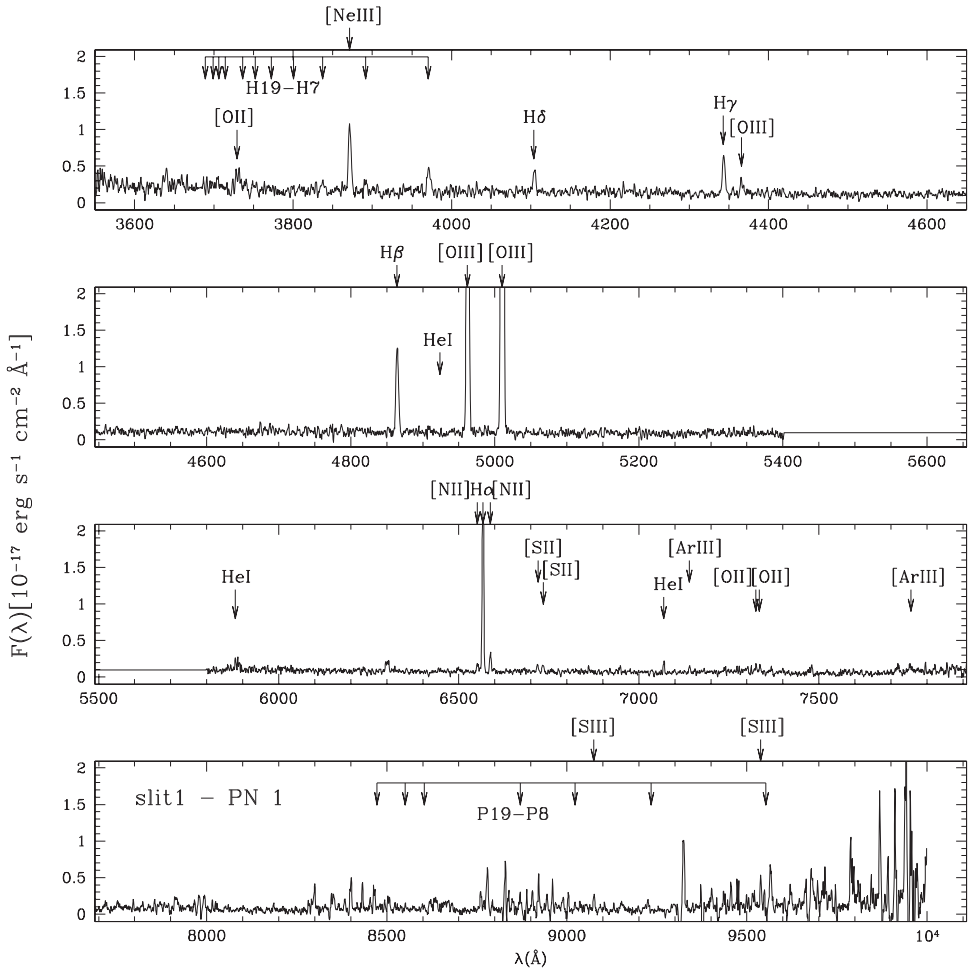

Figure 6. LBT/MODS spectra in the blue and red channels for PN-1 in NGC 4449 with all the identified emission lines indicated. A linear interpolation was performed in the 5400–5800 Å region, where the sensitivities of the blue and red detectors drop. A ∼1 Å boxcar filter smoothing was applied to the spectrum to better highlight the low singal-to-noise ratio features. The spectra of the other PNe (PN-2, PN-3, PN-4, PN-5) are provided in the Appendix.

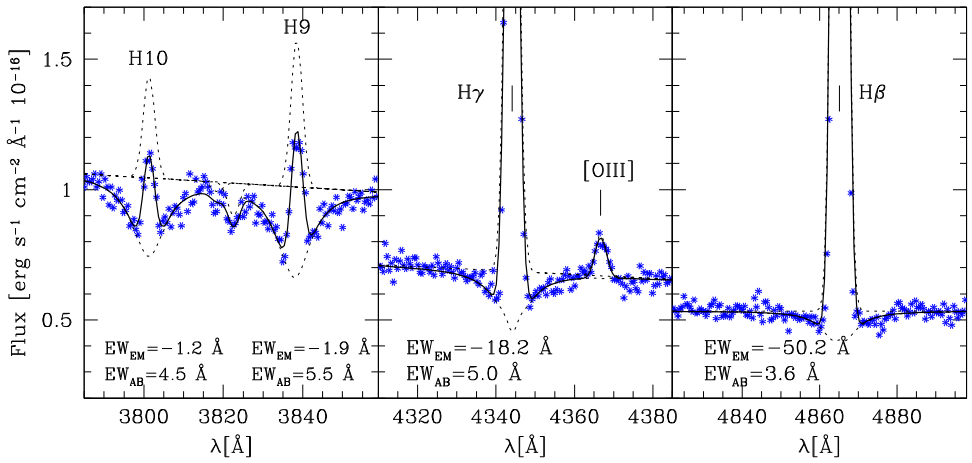

Figure 7. Example (region H II-6) of spectral fit to the regions around some Balmer lines. The asterisks are the observed spectrum, while the solid line is the best fit. The individual components of the fit are plotted with a dashed line: linear continuum, Gaussian profiles for the emission lines, and Voigt profiles for the Balmer absorption lines. The outcome of fit to the H10(λ3798) and H9(λ3835) lines, with prominent absorption wings, was used to fix the Lorentian and Gaussian FWHMs during the fit to redder Balmer lines. The derived Balmer equivalent widths in absorption and in emission are provided within each panel. The absorption feature between H10 and H9 is due to a blend of Fe I lines. The figure clearly shows that the contribution of absorption with respect to emission becomes increasingly lower toward redder wavelengths (see Section 3.1 for more details.).

Table 5. The associated errors were derived by inputting into the *getCrossTemDen* task the $\pm 1\sigma$ interval for each diagnostic line flux ratio.

The availability of multiple T_e measurements in H II regions allowed us to investigate the comparison between temperatures measured for different ions (O^+, O^{+2}, S^{+2}). The behavior of

Table 4
Used Atomic Data Set

Ion	Emissivities	
H^+	Storey & Hummer (1995)	
He^+	Porter et al. (2012, 2013)	
He^{+2}	Storey & Hummer (1995)	
	Transition Probabilities	Collision Strengths
N^+	Galavis et al. (1997), Wiese et al. (1996)	Tayal (2011)
O^+	Zeippen (1982), Wiese et al. (1996)	Pradhan et al. (2006), Tayal (2007)
O^{+2}	Storey & Zeippen (2000), Wiese et al. (1996)	Aggarwal & Keenan (1999)
S^+	Podobedova et al. (2009)	Tayal & Zatsarinny (2010)
S^{+2}	Podobedova et al. (2009)	Tayal & Gupta (1999)
Ne^{+2}	Galavis et al. (1997)	McLaughlin & Bell (2000)
Ar^{+2}	Mendoza (1983), Kaufman & Sugar (1986)	Galavis et al. (1995)

T_e[S III] against T_e[O III] and of T_e[O II] against T_e[O III] for our H II regions is shown in Figure 8, together with the predicted correlations from Garnett (1992) and Izotov et al. (2006) based on photoionization models. The derived temperatures are consistent, within the errors, with the predictions from the models, although they do not exhibit clear correlations, probably because of the small temperature range sampled by our data. In particular, we notice that the data points in the T_e[O II] versus T_e[O III] diagram exhibit a large scatter around the theoretical relations, an effect that was also found and discussed by other authors (e.g., Kennicutt et al. 2003; Bresolin et al. 2009a; Berg et al. 2015). A detailed discussion of the possible theoretical and observational causes of this disagreement (e.g., recombination contribution to the [O II]$\lambda\lambda$7320, 7330 lines, radiative transfer and shocks affecting the [O II] lines, reddening uncertainties) can be found in these studies. We notice that our [O II] temperatures are affected by large observational errors, both because of the uncertain flux calibration below ~4000 Å, as discussed in Section 2, and because of the large uncertainty in the extinction-corrected [O II] ratios, due to the large wavelength difference between the [O II] $\lambda\lambda$3726, 3729 doublet and the [O II]$\lambda\lambda$7320, 7330 complex.[7]

Chemical abundances were derived assuming a three-zone model for the electron temperature structure: the [O III] temperature was adopted for the highest-ionization zone (O^{+2}, Ne^{+2}, He^+, He^{+2}), the [S III] temperature for the intermediate-ionization zone (S^{+2}, Ar^{+2}), and the [O II] temperature for the low-ionization zone (O^0, O^+, N^+, S^+, Fe^{+2}). For T_e[O III] and T_e[S III], we used the temperatures directly derived from the [O III] λ4363/$\lambda\lambda$4959, 5007 and [S III]λ6312/$\lambda\lambda$9069, 9532 line ratios. For the [O II] temperature, instead, in view of the problems observed in the T_e[O II] versus T_e[O III] plane, we used the relation from Garnett (1992):

$$T_e[\mathrm{O\,II}] = 0.70 \times T_e[\mathrm{O\,III}] + 3000\ \mathrm{K}, \quad (3)$$

[7] The [O II]$\lambda\lambda$7320, 7330 complex consists in fact of the blend of the two [O II]$\lambda\lambda$7319, 7320 lines and of the blend of the two [O II] $\lambda\lambda$7330, 7331 lines.

an approach that is widely applied in the literature to reduce the uncertainty in the [O II] temperature determination (e.g., Kennicutt et al. 2003; Bresolin 2011; Berg et al. 2015). However, we caution that the errors on the [O II] temperature derived with this model-based relation are formal errors obtained by propagating the T_e[O III] uncertainties, without assigning any error to the temperature calibration itself; as a consequence, the errors on T_e[O II] may be underestimated, a problem that has been discussed by previous studies (e.g., Hägele et al. 2006).

To determine the abundances of the various ions, we used the extinction-corrected fluxes (listed in Table 2) for the following lines: He I λ4471, He I λ5876, and He I λ6678 for He^+, He II λ4686 (when available) for He^{+2}, [N II] $\lambda\lambda$6548, 6584 for N^+, [O III] $\lambda\lambda$4959, 5007 for O^{+2}, [O II]$\lambda\lambda$3726, 3729 and [O II]$\lambda\lambda$7320, 7330 for O^+, [O I]λ6300 and [O I]λ6364 for O^0, [Ne III] λ3869 for Ne^{+2}, [S II] $\lambda\lambda$6716, 6731 for S^+, [S III] λ6312 and [S III] λ9069 + λ9531 for S^{+2}, [Ar III]λ7136 and [Ar III]λ7751 for Ar^{+2}, and [Fe III]$\lambda\lambda$4986, 4987 for Fe^{+2}. The PyNeb code adopts the He I emissivities of Porter et al. (2012, 2013) including collisional excitation, so no correction to the emission-line fluxes for this effect (Clegg 1987) needs to be applied. The He I λ7065 line, which has a strong contribution from collisional excitation, was not included in the computation of the He^+; in fact, the uncertainties on the derived n_e values translate into large errors on the He^+ abundance due to the strong dependence of the He I λ7065 emissivity on density (see, e.g., Figure 4 of Porter et al. 2012).

To get an estimate of the ion abundance uncertainties, we ran the *getIonAbundance* task for ranges of temperatures, densities, and flux ratios within the $\pm 1\sigma$ levels and conservatively adopted the maximum excursion around the nominal abundance value as our error. When multiple sets of lines were available for a single ion (i.e., He^+, O^+, O^0, S^{+2}, Ar^{+2}), its abundance was computed by averaging all the abundances from the various lines (or line complexes). Typically, the standard deviation around the mean abundance from the different lines is lower than or comparable to the error obtained by propagating the individual abundance uncertainties; conservatively, we adopted the largest value as our uncertainty on the abundance determinations.

Total element abundances were derived from the abundances of ions seen in the optical spectra using ionization correction factors (ICFs). For oxygen, the total abundance was computed as $O/H = (O^+ + O^{+2})/H^+$. From Izotov et al. (2006), the contribution of O^{+3} to the total oxygen abundance is expected to be <1%, since $O^+/(O^+ + O^{+2}) > 0.1$ in our H II regions. We did not add the contribution from O^0 because it is associated with neutral hydrogen, and almost all the emission in the [O I] $\lambda\lambda$6300, 6364 lines comes from photodissociation regions (Abel et al. 2005).

To compute the abundances of the other elements, we adopted the ICFs from Izotov et al. (2006) for the "high"-Z regime ($12 + \log O/H \geqslant 8.2$):

$$\mathrm{ICF}(N^+) = -1.476v + 1.752 + 0.688/v, \quad (4)$$

$$\mathrm{ICF}(Ne^{+2}) = -0.591w + 0.927 + 0.546/w, \quad (5)$$

$$\mathrm{ICF}(S^+ + S^{+2}) = 0.178v + 0.610 + 0.153/v, \quad (6)$$

$$\mathrm{ICF}(Ar^{+2}) = 0.517v + 0.763 + 0.042/v, \quad (7)$$

$$\mathrm{ICF}(Fe^{+2}) = -1.377v + 1.606 + 1.045/v, \quad (8)$$

Table 5
Derived Properties for H II Regions in NGC 4449

Property	H II-1	H II-2	H II-3	H II-4	H II-5	H II-6
R.A. (J2000)	12:28:12.626	12:28:09.456	12:28:17.798	12:28:16.224	12:28:13.002	12:28:13.925
Decl. (J2000)	+44:05:04.35	+44:05:20.35	+44:06:32.49	+44:06:43.32	+44:06:56.38	+44:07:19.04
R/R_{25}	0.20	0.13	0.49	0.46	0.44	0.57
$n_e(\mathrm{cm}^{-3})$	50^{+30}_{-30}	120^{+100}_{-90}	40^{+70}_{-40}	70^{+100}_{-70}	40^{+100}_{-40}	30^{+100}_{-30}
$T_e(\mathrm{O}^+)$ (K)	10300 ± 900	9100 ± 800	⋯	9000 ± 1000	10000 ± 1000	9000 ± 1000
$T_e(\mathrm{O}^{++})$ (K)	9300 ± 100	9100 ± 200	10000 ± 200	9300 ± 400	9700 ± 300	10600 ± 400
$T_e(\mathrm{S}^{++})$ (K)	9600 ± 100	9800 ± 300	9900 ± 400	9900 ± 600	9700 ± 500	10900 ± 600
$(\mathrm{O}^+/\mathrm{H}^+) \times 10^4$	0.50 ± 0.04	0.88 ± 0.09	1.3 ± 0.2	1.0 ± 0.1	0.9 ± 0.1	1.2 ± 0.2
$(\mathrm{O}^{++}/\mathrm{H}^+) \times 10^4$	2.0 ± 0.1	2.0 ± 0.2	0.75 ± 0.06	1.4 ± 0.2	1.3 ± 0.1	0.9 ± 0.1
$12 + \log(\mathrm{O/H})$	8.40 ± 0.02	8.46 ± 0.03	8.32 ± 0.03	8.39 ± 0.04	8.34 ± 0.04	8.32 ± 0.04
(He/H)	0.089 ± 0.003	0.090 ± 0.005	0.084 ± 0.004	0.092 ± 0.008	0.086 ± 0.006	0.095 ± 0.007
$(\mathrm{N}^+/\mathrm{H}^+) \times 10^6$	1.96 ± 0.06	3.1 ± 0.3	5.2 ± 0.5	3.7 ± 0.6	3.1 ± 0.4	6.6 ± 0.8
$12 + \log(\mathrm{N/H})$	6.99 ± 0.01	7.04 ± 0.04	6.99 ± 0.04	7.02 ± 0.07	6.95 ± 0.05	7.15 ± 0.05
$(\mathrm{Ne}^{++}/\mathrm{H}^+) \times 10^5$	4.8 ± 0.3	3.9 ± 0.4	1.5 ± 0.1	3.4 ± 0.6	2.3 ± 0.3	3.0 ± 0.4
$12 + \log(\mathrm{Ne/H})$	7.74 ± 0.02	7.71 ± 0.04	7.52 ± 0.04	7.71 ± 0.08	7.53 ± 0.06	7.76 ± 0.06
$(\mathrm{S}^+/\mathrm{H}^+) \times 10^7$	4.1 ± 0.1	3.9 ± 0.4	14 ± 1	7 ± 1	7.2 ± 0.9	20 ± 2
$(\mathrm{S}^{++}/\mathrm{H}^+) \times 10^6$	3.00 ± 0.09	3.3 ± 0.3	2.7 ± 0.3	2.9 ± 0.5	3.4 ± 0.3	2.5 ± 0.3
$12 + \log(\mathrm{S/H})$	6.68 ± 0.01	6.64 ± 0.04	6.60 ± 0.03	6.58 ± 0.06	6.64 ± 0.04	6.65 ± 0.04
$(\mathrm{Ar}^{++}/\mathrm{H}^+) \times 10^7$	8.8 ± 0.5	9.3 ± 0.6	6.5 ± 0.4	7.4 ± 0.9	9.3 ± 0.9	6.6 ± 0.6
$12 + \log(\mathrm{Ar/H})$	5.98 ± 0.02	5.99 ± 0.03	5.88 ± 0.03	5.90 ± 0.06	6.00 ± 0.04	5.88 ± 0.04
$(\mathrm{Fe}^{++}/\mathrm{H}^+) \times 10^7$	0.74 ± 0.06	1.8 ± 0.2	4.0 ± 0.5	1.7 ± 0.2	2.4 ± 0.5	5.6 ± 0.7
$12 + \log(\mathrm{Fe/H})$	5.69 ± 0.03	5.92 ± 0.04	5.97 ± 0.06	5.79 ± 0.05	5.94 ± 0.09	6.18 ± 0.06

Table 6
Derived Properties for PNe in NGC 4449

Property	PN-1	PN-2	PN-3	PN-5
R.A. (J2000)	12:28:04.126	12:28:03.540	12:28:03.972	12:28:13.950
Decl. (J2000)	+44:04:25.14	+44:04:34.80	+44:05:56.78	+44:07:45.29
R/R_{25}	0.57	0.56	0.43	0.71
n_e (cm^{-3})	600^{+500}_{-400}	300^{+400}_{-300}	1300^{+1000}_{-700}	⋯
$T_e(\mathrm{O}^{++})$ (K)	12200 ± 900	14000 ± 1000	13000 ± 1000	13000 ± 1000
$(\mathrm{O}^+/\mathrm{H}^+) \times 10^5$	0.4 ± 0.1	0.9 ± 0.3	1.2 ± 0.4	0.07 ± 0.02
$(\mathrm{O}^{++}/\mathrm{H}^+) \times 10^4$	2.2 ± 0.5	1.6 ± 0.4	1.7 ± 0.4	1.9 ± 0.4
$12 + \log(\mathrm{O/H})$	8.3 ± 0.1	8.3 ± 0.1	8.4 ± 0.1	8.3 ± 0.1
He/H	0.08 ± 0.02	0.09 ± 0.02	0.08 ± 0.01	0.10 ± 0.02
$(\mathrm{N}^+/\mathrm{H}^+) \times 10^6$	3.4 ± 0.9	3.4 ± 0.9	7 ± 2	1.2 ± 0.3
$12 + \log(\mathrm{N/H})$	8.2 ± 0.1	7.9 ± 0.1	8.2 ± 0.1	8.5 ± 0.1
$(\mathrm{Ne}^{++}/\mathrm{H}^+) \times 10^5$	4 ± 1	2.9 ± 0.9	2.7 ± 0.8	3 ± 1
$12 + \log(\mathrm{Ne/H})$	7.6 ± 0.1	7.5 ± 0.1	7.6 ± 0.1	7.5 ± 0.1
$(\mathrm{S}^+/\mathrm{H}^+) \times 10^7$	4 ± 1	2.9 ± 0.8	3.2 ± 0.9	⋯
$(\mathrm{S}^{++}/\mathrm{H}^+) \times 10^6$	1.8 ± 0.7	2.0 ± 0.8	1.6 ± 0.7	⋯
$12 + \log(\mathrm{S/H})$	6.8 ± 0.1	6.6 ± 0.2	6.6 ± 0.2	⋯
$(\mathrm{Ar}^{++}/\mathrm{H}^+) \times 10^7$	4.5 ± 1.3	8 ± 2	4 ± 1	⋯
$12 + \log(\mathrm{Ar/H})$	5.9 ± 0.1	6.2 ± 0.1	5.9 ± 0.1	⋯

Table 7
The Total Sample of 28 PNe

ID	m_{F555W} (Vega mag)	m_{F502N} (Vega mag)	$(M - M^*)_{[O\ III]}$ (mag)	ID	m_{F555W} (Vega mag)	m_{F502N} (Vega mag)	$(M - M^*)_{[O\ III]}$ (mag)
PN-1	23.86	⋯	0.82	PN-15	25.41	22.85	2.36
PN-2	24.39	⋯	1.01	PN-16	25.49	23.10	2.44
PN-3	24.46	22.03	1.25	PN-17	24.57	22.00	1.52
PN-4	24.78	22.6	0.57	PN-18	23.82	21.85	0.77
PN-5	24.26	⋯	1.01	PN-19	23.38	21.83	0.33
PN-6	24.33	22.02	1.28	PN-20	23.63	21.60	0.58
PN-7	24.47	22.38	1.42	PN-21	24.27	22.69	1.22
PN-8	25.11	22.72	2.06	PN-22	24.89	22.19	1.84
PN-9	24.62	22.48	1.57	PN-23	24.34	21.89	1.29
PN-10	24.51	22.18	1.46	PN-24	23.29	21.30	0.24
PN-11	24.20	21.85	1.15	PN-25	25.15	23.16	2.10
PN-12	23.96	21.56	0.91	PN-26	24.70	21.99	1.65
PN-13	23.93	21.57	0.88	PN-27	23.09	20.75	0.04
PN-14	25.59	22.93	2.54	PN-28	24.97	22.30	1.92

Note. Apparent m_{F555W} and m_{F502N} magnitudes derived for our sample of 28 PNe from *HST*/ACS data. The $(M - M^*)_{[O\ III]}$ magnitude difference for PN-1 to PN-5 is obtained from the observed [O III] fluxes listed in Table 3 (corrected for the distance modulus), by assuming $M^*_{[O\ III]} = -4.36$ as the PN cutoff magnitude. For the remaining objects, we nominally assume $m_{[O\ III]} = m_{F555W} + 0.5$, as explained in the text.

where

$$v = O^+/(O^+ + O^{+2}),\ w = O^{+2}/(O^+ + O^{+2}). \quad (9)$$

In H II-6, where the He II λ4686 nebular emission line was clearly detected (see Figure 20 in Appendix A), the He abundance was computed as $He^+ + He^{+2}$ (with He^{+2} contributing ∼1% to the total He abundance), while we neglected the He^{+2} contribution in all the other H II regions. We notice that a modest nebular He II λ4686 emission could be present in H II-1, superimposed on a much stronger W-R broad emission component (see Section 5 and Table 2); however, since this nebular He II contribution turns out to be very small and is furthermore affected by large uncertainties due to the dominating W-R component, we decided to neglect it in the computation of the total He abundance for region H II-1.

To derive the total abundance of He, one should in principle account for the ionization structure of the nebula. In fact, the radius of the He^+ zone can be smaller than the radius of the H^+ zone in the case of soft ionizing radiation, or larger in the case of hard radiation. In the former case, a correction for unseen neutral helium needs to be applied, resulting in an ionization correction factor $ICF(He^+ + He^{+2}) > 1$ (Izotov et al. 2007). Izotov et al. (2013) ran photoionization models to investigate the behavior of $ICF(He^+ + He^{+2})$ as a function of metallicity and excitation parameter w. According to their "high"-Z models, $ICF(He^+ + He^{+2})$ approaches unity for large w values and ICF ∼ 1.03 for $w \sim 0.3$. Since $w > 0.3$ in our H II regions, it is reasonable to neglect this correction.

4.2. Planetary Nebulae

Densities and temperatures of PNe were derived using the density-sensitive [S II]λ6716/λ6731 line ratio and the temperature-sensitive [O III] λ4363/$\lambda\lambda$4959 + 5007 ratio. Figure 3 shows that the [O III] λ4363 line was detected in all five PNe. We excluded PN 4 from our study since its 2D spectra appeared highly contaminated from diffuse emission owing to nearby H II regions. For all the other PNe, we obtained [O III] temperatures in the range of 12,000–14,000 K. Densities were derived for PN 1, PN 2, and PN 3 with large errors ($n_e = 600^{+500}_{-400}$, 300^{+400}_{-300}, 1300^{+1000}_{-700} cm^{-3}), while for PN 5, where the [S II]$\lambda\lambda$6716, 6731 lines were not detected, we assumed $n_e = 1000$ cm^{-3}. Following the same approach adopted by many studies in the literature (e.g., Stasińska et al. 2013; Idiart et al. 2007), we assumed that the temperature of all the ions is equal to T_e[O III]. In fact, empirical relations between T_e[O III] and T_e[N II] derived in the literature for PNe (Kaler 1986; Kingsburgh & Barlow 1994; Wang & Liu 2007) show important spreads and have different trends.

For all the PNe but PN 4, we derived the abundances of He^+, N^+, O^+, O^{+2}, and Ne^{+2} from the He I λ5876, [N II] $\lambda\lambda$6548, 6584, [O II] $\lambda\lambda$3726, 3729, [O III] $\lambda\lambda$4959, 5007, and [Ne III] λ3869 lines; S^+, S^{+2}, and Ar^{+2} abundances were derived for PN 1, PN 2, and PN 3 from the [S II]$\lambda\lambda$6716, 6731, [S III]λ9069, and [Ar III]λ7136 lines; and He^{+2} abundances were obtained only for PN 2 and PN 3 from the He II λ4686 line. For these two PNe, the total He abundance was computed as $He^+ + He^{+2}$, while the He^{+2} contribution was omitted for PN 1 and PN 5.

To derive total element abundances, we used the ICFs from Kingsburgh & Barlow (1994, hereafter KB94). For oxygen, the correction due to unseen O^{+3} is

$$ICF(O^+ + O^{++}) = \left(\frac{He^+ + He^{+2}}{He^+}\right)^{2/3}. \quad (10)$$

The absence of He II lines in PN 1 and PN 5 indicates negligible He^{+2} abundances, and thus we do not expect an important amount of O^{+3} in these two objects. On the other hand, we derived $ICF(O^+ + O^{++}) \sim 1.1$ and ∼1.4 for PN 2 and PN 3, respectively.

For the other elements, the KB94 ICFs are

$$ICF(N^+) = \frac{O}{O^+}, \quad (11)$$

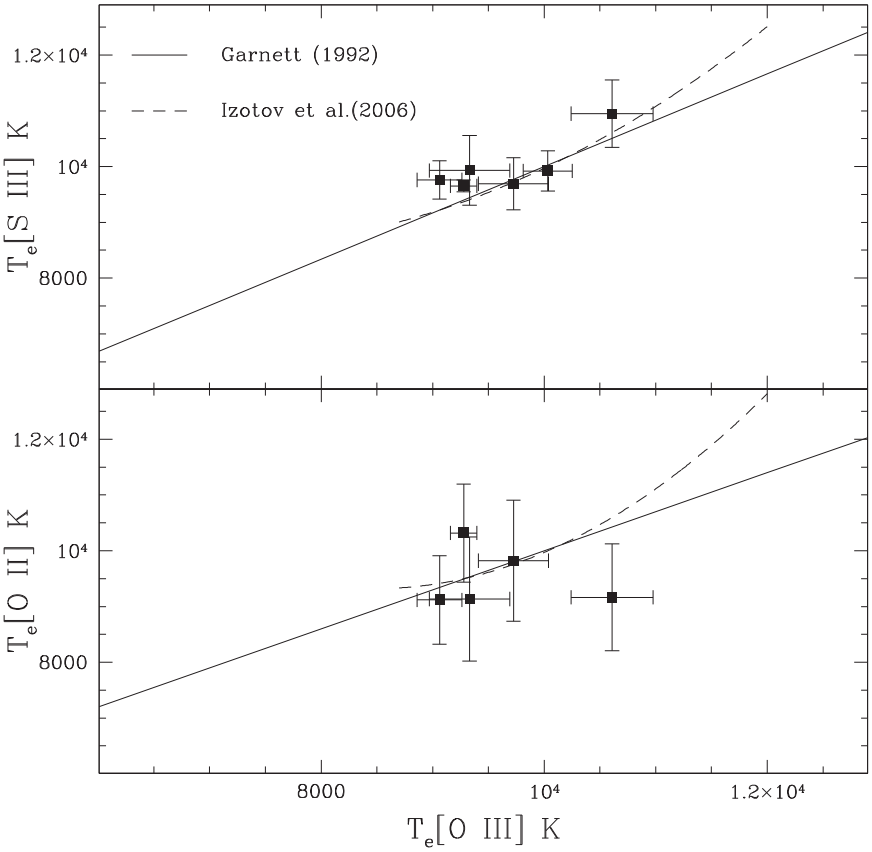

Figure 8. Correlations between electron temperatures derived for H II regions in NGC 4449 through different diagnostics: [O III]λ4363/[O III]$\lambda\lambda$4959, 5007 for T_e[O III], [S III]λ6312/[S III]$\lambda\lambda$9069, 9532 for T_e[S III], and [O II]$\lambda\lambda$3726, 3729/[O II]$\lambda\lambda$7320, 7330 for T_e[O II]. The solid and dashed lines are the predicted correlations based on photoionization models from Garnett (1992) and Izotov et al. (2006), respectively.

$$\mathrm{ICF(Ne^{++})} = \frac{\mathrm{O}}{\mathrm{O^{+2}}}, \tag{12}$$

$$\mathrm{ICF(Ar^{++})} = 1.87, \tag{13}$$

$$\mathrm{ICF(S^{+} + S^{++})} = \left[\left(1 - \frac{\mathrm{O^{+}}}{\mathrm{O}}\right)^{3}\right]^{-1/3}. \tag{14}$$

The derived PN abundances are provided in Table 6.

Recently, a new set of ICFs was presented by Delgado-Inglada et al. (2014, hereafter DMS14). The new ICFs from DMS14 are based on a large grid of photoionization models and provide significant improvement with respect to previous ICFs for PNe. We present in Appendix C a description of the new ICFs and evaluate the effect on the derived PN abundances. We find that oxygen is very little affected by the new ICFs, with abundance differences of only a few percent in dex. For the other elements, i.e., N, Ne, S, and Ar, the difference in abundance is larger than for O, but always within $\sim$0.1 dex, comparable to the errors associated with our derived abundances.

5. Wolf-Rayet Features

According to stellar evolution models, the most massive stars ($M \gtrsim 20\,M_{\odot}$, for a solar-metallicity model with rotation; see Meynet & Maeder 2005) evolve into the W-R phase $\approx$2–5 Myr after their birth. A W-R star is a bare stellar core that has lost the main part of its H-rich envelope via strong winds (e.g., Maeder 1991; Maeder & Conti 1994), or by mass transfer through the Roche lobe in close binary systems (e.g., Chiosi & Maeder 1986). The characteristic features of W-R stars are broad emission lines of helium, nitrogen, carbon, and oxygen formed in the high-velocity wind region surrounding the hot stellar photosphere. In the optical, two main emission features can be identified: the so-called *blue bump* around 4600–4700 Å, and the *red bump* centered around 5800 Å, usually fainter than the blue bump. The blue bump is due to the blend of a broad He II λ4686 emission feature with N III λ4640 (WN subtype) or with C III λ4652 (WC subtype). The red bump is due to the C IV λ5808 emission in WC stars and is more rarely observed than the blue bump. The WN and WC subtypes represent an evolutionary sequence since the ejection process is believed to occur in succession, first exposing the surface mainly composed of the nitrogen-rich products of the CNO cycle (WN stars), and later the carbon-rich layer due to He burning (WC and WO; Dray et al. 2003, and references therein).

We detected the blue bump in two (H II -1 and H II -4) out of the six H II regions studied in NGC 4449. On the other hand, the wavelength range of the red bump falls close to the region of low sensitivity of the blue and red MODS detectors, preventing us from drawing conclusions about the presence of this feature. The blue bump spectral region in H II-1 and H II-4 was modeled by simultaneously fitting the W-R features (N III λ4640, C III λ4652, He II λ4686) and the nebular emission lines ([Fe III] λ4658, He II λ4686, [Ar IV] + He I λ4713, [Ar IV]λ4740) following an approach similar to that of Brinchmann et al. (2008). To evaluate the underlying stellar continuum, we performed a spectral energy distribution (SED)

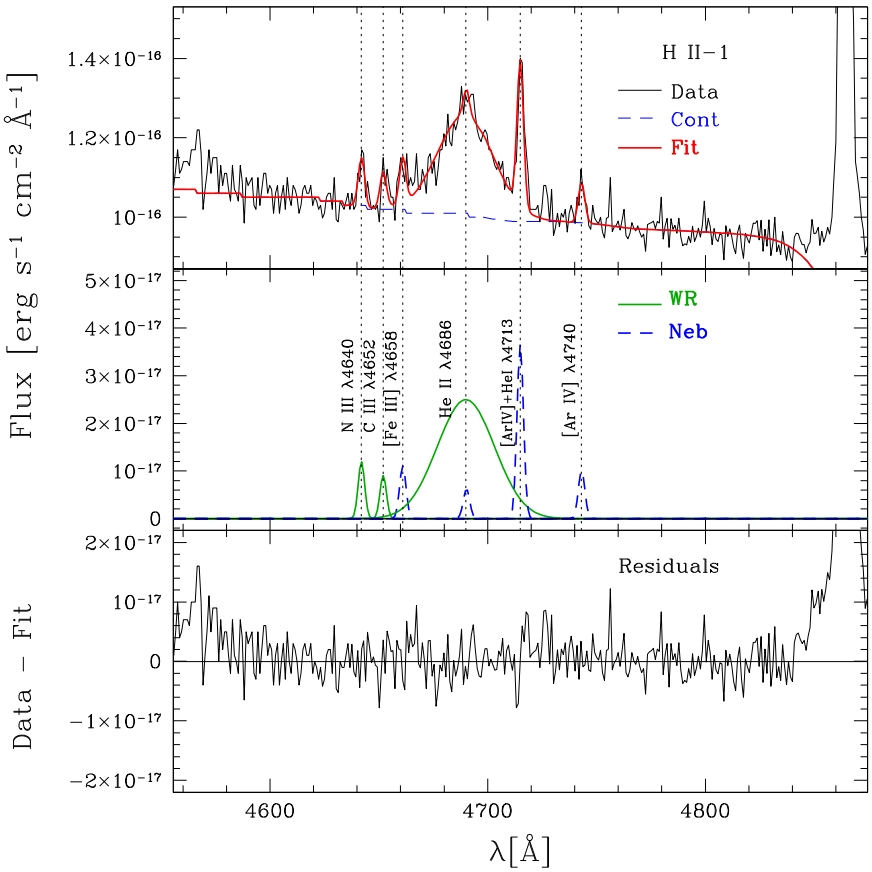

Figure 9. Portion of the spectrum of H II-1 around the region of the W-R blue bump at ∼4690 Å. Top panel: observed spectrum (thin black line) and total (continuum plus emission lines) fit (red thick line). The continuum has been modeled with a $Z = 0.004$, 3–4 Myr old SSP, normalized at 4770–4840 Å (see Section 5 for details). Middle panel: fitted emission lines (solid green line for W-R features, dashed blue line for nebular narrow emission lines). Bottom panel: residual after subtracting the best-fit model.

fit to the 4000–7000 Å range (avoiding the regions contaminated by nebular emission lines) using SSP models from the Padova group (Marigo et al. 2008; Chavez et al. 2009). The SED of H II -1 and H II -4 turned out to be best reproduced by a $Z = 0.004$, 3–4 Myr old population; this result, which we expect to be highly affected by the age–metallicity degeneracy, is not intended to draw conclusions on the physical properties of the underlying stars, but has the mere purpose of providing a reliable continuum below the bump. The fits to the blue bump in regions H II-1 and H II-4 are shown in Figures 9 and 10, respectively. We fixed the nebular emission lines to have the same Gaussian widths as the other emission lines in the 4000–6000 Å spectral range (FWHM ∼ 4 Å), while the FWHMs of the W-R features were allowed to vary as free parameters.

For region H II-1, the width of the broad He II λ4686 feature is best fitted with a Gaussian FWHM of ∼30 Å, corresponding[8] to a velocity $\sigma \sim 800\,\mathrm{km\,s^{-1}}$; the presence of a nebular contribution to this line is not well constrained given the large errors (see Table 2). Surprisingly, the N III λ4640 and C III λ4652 features show widths comparable to those of the nebular emission lines. A similar result was found by Smith et al. (2016) when fitting the W-R blue bump for cluster #5 in the blue compact dwarf galaxy NGC 5253; as they noticed, the narrow widths derived for N III and C III would suggest that these lines are likely to be nebular in origin, although detecting these transitions is unusual.

For region H II-4, it was necessary to assume two broad emission components to obtain a satisfactory fit to the He II λ4686 feature: our best fit provides two Gaussians with FWHMs of ∼8 Å and ∼45 Å, corresponding to velocities of $\sim 200\,\mathrm{km\,s^{-1}}$ and $\sim 1200\,\mathrm{km\,s^{-1}}$, while the N III and C III features are reproduced by two Gaussians with FWHM ∼ 8 Å. Notice that wind velocities derived in W-R stars can be as high as $\sim 2500\,\mathrm{km\,s^{-1}}$ (e.g., Niedzielski & Skorzynski 2002).

We show in Figure 11 a comparison of the W-R features in H II-1 and H II-4 against the Starburst99 instantaneous burst models (Leitherer et al. 2014). For region H II-1, we do not show the ratios involving the C III and N III emission because, as previously discussed, the narrow widths derived for these lines would suggest that they are nebular in origin and not due to W-R stars. The plotted models were computed with the Geneva $Z = 0.008$ stellar tracks (Schaller et al. 1992; Meynet et al. 1994) assuming either a standard mass-loss (SML) or a high mass-loss (HML) rate. It is well known that models of massive stars suffer uncertainties due to rotation (e..g Meynet & Maeder 2005) and to possible binary evolution (e.g., Vanbeveren et al. 2007; Eldridge et al. 2008). Models including rotation have been computed by the Geneva group for some metallicities, but are not available for $Z = 0.008$.

Figure 11 shows that W-R features (mainly C III, N III, and He II λ4686) are visible during a limited age range, from ≈1 to ≈4.5 Myr in the case of SML models, and up to ≈6 Myr for HML models. While the N III emission is always present during the W-R phase, the C III emission due to the later appearance of WC stars is observed only after ≈3 Myr (top panel of Figure 11).

[8] Computed as $\sigma = \frac{\sqrt{\mathrm{FWHM}^2 - \mathrm{FWHM}^2_{\mathrm{instr}}}}{2.35} \times \frac{c}{\lambda}$, where FWHM and $\mathrm{FWHM}_{\mathrm{instr}}$ are the measured and the instrumental widths, respectively.

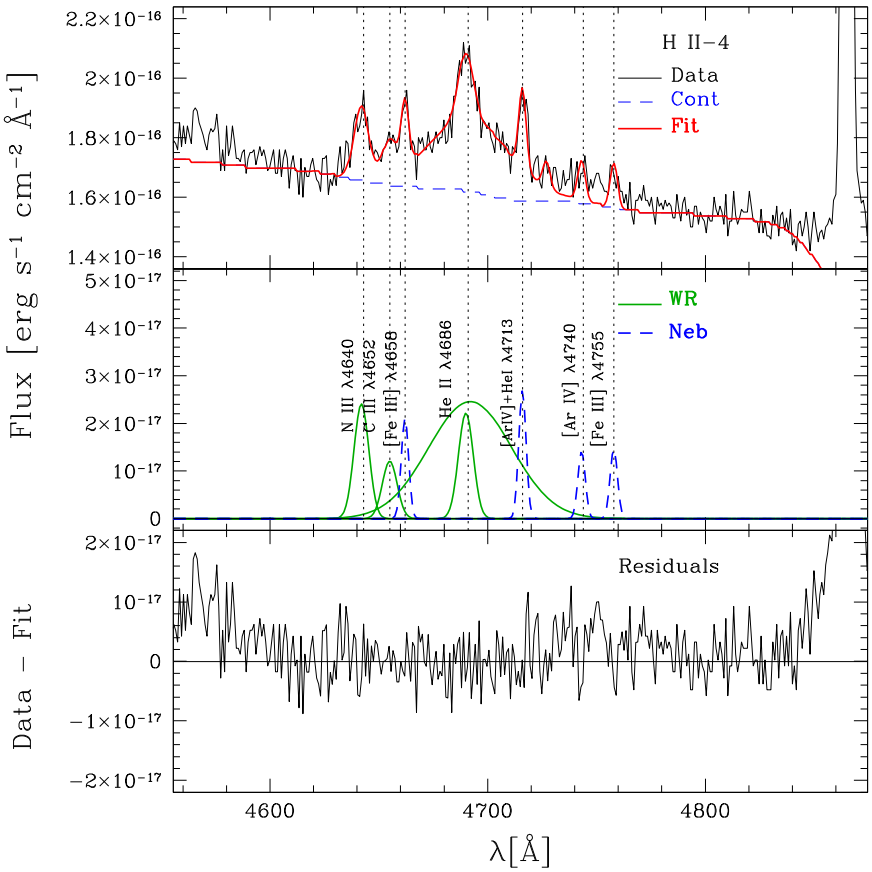

Figure 10. Same as in Figure 9, but for H II-4.

This holds both for the SML and for the HML models, although we notice that the latter ones imply significantly higher F(C III)/F(N III) ratios. The presence of broad C III emission in H II-4 indicates the existence of a W-R population at least ≈3 Myr old. The behavior of the F(He II λ4686)/F(N III) ratio is displayed in the middle panel of Figure 11. The SML and HML models predict a moderate difference in this ratio. The F(He II)/F(N III) ratio is as high as ∼10 in the earliest phases and then rapidly decreases after ∼3 Myr, reaching down to ∼2. For H II-4, we derive a ratio of $\sim 6 \pm 2$, compatible with an age of ∼3 Myr. Finally, the bottom panel of Figure 11 shows the evolution of the F(He II λ4686)/F(Hβ) ratio, which is proportional to the number of W-R stars over the number of ionizing OB stars. Here the difference between the two sets of models is striking: while the SML model largely underpredicts the number of W-R over OB stars, the HML model provides a very satisfactory match for ages older than ≈4 Myr for both H II-1 and H II-4. This is in agreement with past studies in the literature showing that the observed properties of W-R stars require, in absence of stellar models with rotation, the inclusion of an enhanced mass loss (e.g., Schaerer & Maeder 1992; Schaller et al. 1992). However, we caution that the difficulty of the models in reproducing the strength of the blue bump could be due to the presence of stars other than "classical" W-R, such as massive, mass-losing core-hydrogen-burning stars close to the main sequence, a stellar phase not yet accounted for in the evolution models (Leitherer et al. 2017). Using the HML models, we derive, from the observed He II λ4686 flux, a number of W-R stars of ≈4 and $\approx 8 \pm 2$ in regions H II-1 and H II-4, respectively.

6. Results on the Chemical Abundances and Abundance Ratios

Element abundances derived in H II regions and PNe are given in Tables 5 and 6. The oxygen abundance interval spanned by our sample is $8.3 \pm 0.1 \leqslant 12 + \log(\mathrm{O/H}) \leqslant 8.46 \pm 0.03$, with average O abundances for H II regions and PNe of 8.37 ± 0.05 and 8.3 ± 0.1, respectively. The H II region results are consistent with previous literature measurements based on the direct temperature method: Talent (1980; see also Skillman et al. 1989) derived an average oxygen abundance of $12 + \log(\mathrm{O/H}) = 8.31 \pm 0.07$ for H II regions in NGC 4449; later, Berg et al. (2012) obtained new MMT spectra for the bright H II knot located a few arcseconds to the south of our H II-6 region (slit 10 in Figure 1) and found an average abundance of $12 + \log(\mathrm{O/H}) = 8.20 \pm 0.08$, consistent with our value of $12 + \log(\mathrm{O/H}) = 8.32 \pm 0.04$ within the errors.

The trend of H II region and PN abundance ratios versus total oxygen abundance is illustrated in Figure 12. We find that, within the oxygen interval spanned by our data, the Ne/O, S/O, and Ar/O ratios are similar for the H II region and PN subsamples and are compatible, within the errors, with a constant trend as a function of oxygen (Figures 12(b)–(d)). This behavior is consistent with what is commonly observed in other studies (e.g., Richer & McCall 2007; Bresolin et al. 2010; Stasińska et al. 2013; Annibali et al. 2015). The explanation is that α-elements are all synthesized by massive stars on similar timescales; thus, their abundance variations occur in lockstep, keeping the corresponding ratios constant. The similarity between the Ne/O, S/O, and Ar/O ratios measured in PNe and H II regions is not surprising since α-elements are

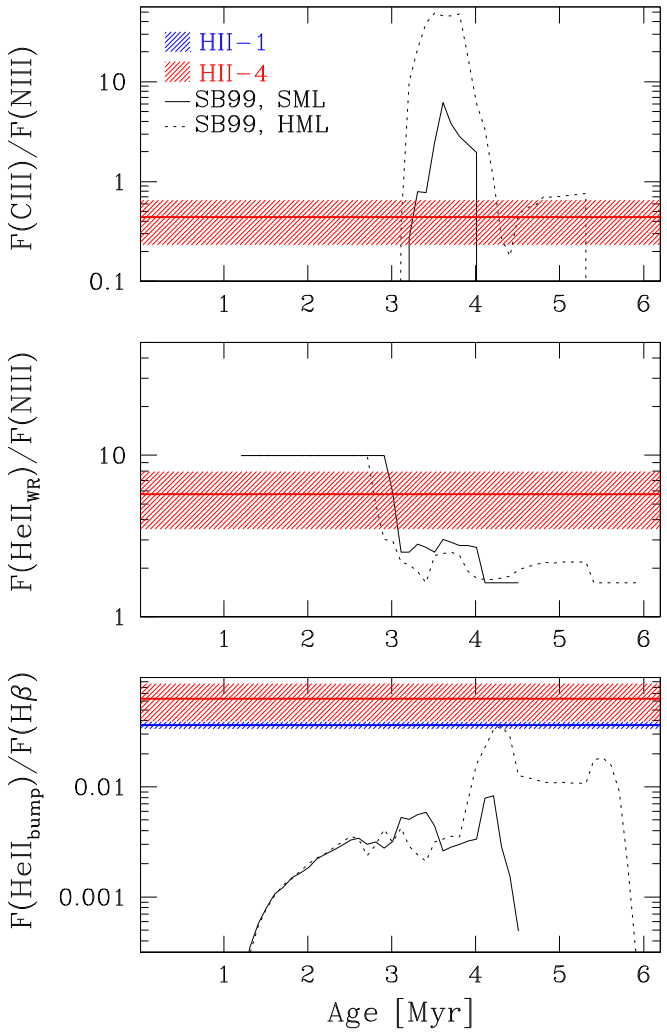

Figure 11. W-R features detected in regions H II-1 and H II-4 against Starburst 99 (SB99) models. The models are based on the Geneva tracks with metallicity $Z = 0.008$ with an SML prescription (solid line) and with an HML prescription (dotted line). From top to bottom: F(C III)/F(N III), F(He II$_{WR}$)/F(N III), and F (He II$_{WR}$)/F(Hβ) ratios vs. age. Notice that the F(He II$_{WR}$) flux refers to the broad W-R component without the contribution from the nebular He II emission line.

not significantly affected during the evolution of low- and intermediate-mass stars. In NGC 4449, the average values of $\langle \log(\mathrm{Ne/O}) \rangle \simeq -0.73$, $\langle \log(\mathrm{S/O}) \rangle \simeq -1.72$, and $\langle \log(\mathrm{Ar/O}) \rangle \simeq -2.40$ are consistent with typical abundance ratios derived in H II regions of star-forming dwarf galaxies (see Figure 13 of Annibali et al. 2015, for NGC 1705).

The major abundance difference between H II regions and PNe is observed for nitrogen (Figure 12(a)), showing a dichotomy in the N/O distribution. Our H II regions exhibit an average $\langle \log(\mathrm{N/O})_{\mathrm{H\,II}} \rangle \simeq -1.35$, comparable to values measured in H II regions of luminous dwarf galaxies (e.g., Kobulnicky & Skillman 1996; Berg et al. 2012) and of spirals for similar oxygen abundances as in NGC 4449 (e.g., Bresolin et al. 2009a; Berg et al. 2015; Croxall et al. 2016). On the other hand, our PNe are more than ≃1 dex enhanced in N with respect to H II regions, with an average $\langle \log(\mathrm{N/O})_{\mathrm{PNe}} \rangle \simeq -0.12$. This is not unusual since previous studies have shown that PNe in nearby galaxies are enriched in N with respect to H II regions; there is a large scatter in the amount of the enrichment, with N/O ratios from close to those measured in H II regions up to ≈1 dex higher (e.g., Peña et al. 2007; Richer & McCall 2007, 2008; Bresolin et al. 2010; Stasińska et al. 2013; García-Rojas et al. 2016). Highly N-enriched PNe are found both in star-forming galaxies and in quiescent early-type galaxies, where star formation ceased a long time ago (e.g., Richer & McCall 2008). However, we notice that our PNe, despite their significant N enrichment, do not appear to be enhanced in He (Figure 12(f)); to our knowledge, there are no models that can simultaneously increase the N abundance by a factor of 10 and leave He unchanged (see, e.g., Karakas & Lattanzio 2007). A possible explanation is that our derived PN He abundances are uncertain because the detected He I λ5876 line is significantly fainter than two nearby sky lines at $\lambda \sim 5867$ Å and $\lambda \sim 5890$ Å.

From the theoretical point of view, the N/O enhancement in PNe is the natural consequence of nitrogen being mostly synthesized in intermediate-mass stars, which are the PN progenitors, and brought to the stellar surface during dredge-up episodes occurring in the RGB and AGB phases; a significant N production may also occur in the most massive and luminous AGB stars through HBB (see Section 1). PNe exhibiting the most extreme N (and He) abundances, classified as type I, are thought to be the descendants of massive ($>3\,M_{\odot}$), relatively young (age $\lesssim$ 400 Myr) AGB stars experiencing HBB (e.g., Corradi & Schwarz 1995; Stanghellini et al. 2006). Torres-Peimbert & Peimbert (1997) proposed $\log(\mathrm{N/O}) > -0.42$ and He/H > 0.105 as an empirical criterion to select type I systems; three PNe out of four in our sample satisfy the condition in N/O, but their helium abundances are similar to those of H II regions around He/H $\simeq 0.09$ (see Figure 12(f)), which cannot be explained with existing models. Although the reliability of the derived He abundances for our PNe could be questioned as discussed before, a strong selection bias should be invoked to explain why a fraction as high as 3/4 of our sample derives from massive star progenitors.

We find no significant trends in the N/O versus O/H distribution of Figure 12(a). Historically, the absence of a trend in N/O versus O/H for low-metallicity systems was taken as the first indication that nitrogen cannot be a pure secondary element. Primary elements (like He, C, and O) are those whose production can start already in stars with primordial initial chemical composition. Secondary elements are those that can be synthesized only if the star already contains their seed elements at birth or at the evolutionary phase when the physical conditions allow the element to be synthesized. As a natural consequence, the abundance of secondary elements is predicted to increase as the square of primary ones (Tinsley 1980). Hence, had N been of fully secondary nature, its ratio to oxygen should have been proportional to the O abundance. Since N/O is instead always found to be quite independent of O/H in the nebulae of individual galaxies (see, e.g., Diaz & Tosi 1986), a significant fraction of N must be of primary origin. In practice, its nature depends on whether the C used to synthesize N was produced by previous nuclear reactions in the same star or was already present in its initial chemical composition. An inspection of the chemical yields computed for low- and intermediate-mass stars (see, e.g., Karakas 2010; Ventura et al. 2013; Vincenzo et al. 2016) shows that N is mainly of secondary origin above a metallicity ≈half of solar and is mainly produced by $M \gtrsim 3.5\,M_{\odot}$ stars experiencing HBB (see also Figures 1 and 2 in Romano et al. 2010). In massive stars N can have a significant primary origin if their metallicity is low and they rotate sufficiently fast (Meynet & Maeder 2002).

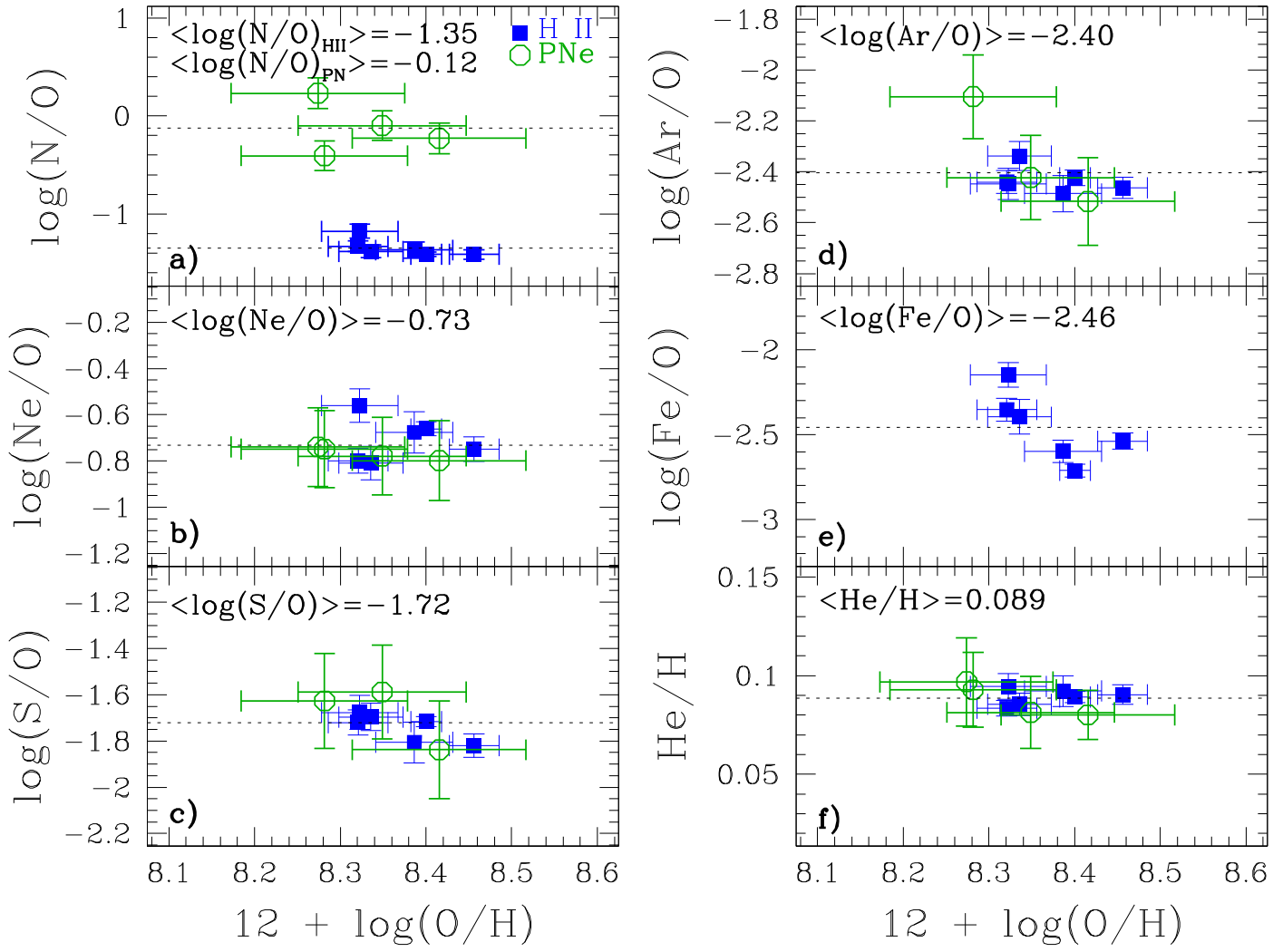

Figure 12. Abundance ratios as a function of total oxygen abundance. Filled and open symbols are for H II regions and PNe, respectively. Within each panel, the label and the dotted horizontal line indicate the average value for the combined H II region and PN data; only in panel (a) are separate log(N/O) mean values for H II regions and PNe provided.

Finally, the distribution of the Fe abundance, derived only for H II regions, is shown in Figure 12(e). The Fe/O ratio shows no clear trend with oxygen; in fact, although there is a hint for an Fe/O decrease with increasing O abundance, in agreement with the behavior revealed by other studies (e.g., Izotov et al. 2006; Delgado-Inglada et al. 2011; Guseva et al. 2011) and commonly interpreted as Fe depletion into dust grains, the range in oxygen abundance probed by our data is likely too small to claim a clear trend. In particular, we notice that the data in the Fe/O versus O plane shown by Delgado-Inglada et al. (2011) span an oxygen interval of almost ∼2 dex, compared to a range of only ∼0.2 dex for the NGC 4449 data. Our Fe and O abundances nicely fall on the region occupied by H II regions in the Delgado-Inglada et al. (2011) plot.

7. Results on the Abundance Spatial Distributions

The behavior of element abundances as a function of galactocentric distance is shown in Figure 13. For immediate comparison between NGC 4449 and other literature studies, the radial distance is expressed in terms of R/R_{25}, where the optical isophotal radius $R_{25} = 3.'1$ is taken from Pilyugin et al. (2015) and corresponds to ≈3.4 kpc at NGC 4449's distance of ≈3.8 Mpc.

Figure 13(a) shows that H II regions and PNe exhibit similar oxygen abundances in the galactocentric distance range of overlap, despite the fact that they represent different evolutionary stages of the galaxy. The same result was found for other star-forming dwarf and spiral galaxies by previous studies reporting similar abundances for H II regions and bright PNe (e.g., Richer 1993; Magrini et al. 2005; Richer & McCall 2007; Bresolin et al. 2010; Stasińska et al. 2013). From the analysis of the CMD of the resolved stars, we know that NGC 4449 has been actively forming stars over the past 1 Gyr (Annibali et al. 2008; McQuinn et al. 2010; Sacchi et al. 2017); therefore, we would expect a significant chemical enrichment since the PN progenitors were formed, i.e., since ∼100 Myr ago or more. On the other hand, the similarity in oxygen abundance between H II regions and PNe suggests that this is not the case. The galactic outflow observed in NGC 4449 (Della Ceca et al. 1997; Summers et al. 2003; Bomans & Weis 2014) may have played an important role, expelling the recently produced α-elements. Accretion of metal-poor gas or acquisition of smaller gaseous systems may have also contributed to dilute the metals in the ISM.

Figure 13(a) illustrates that both H II regions and PNe show a well-defined oxygen gradient. We thus combined H II and PN

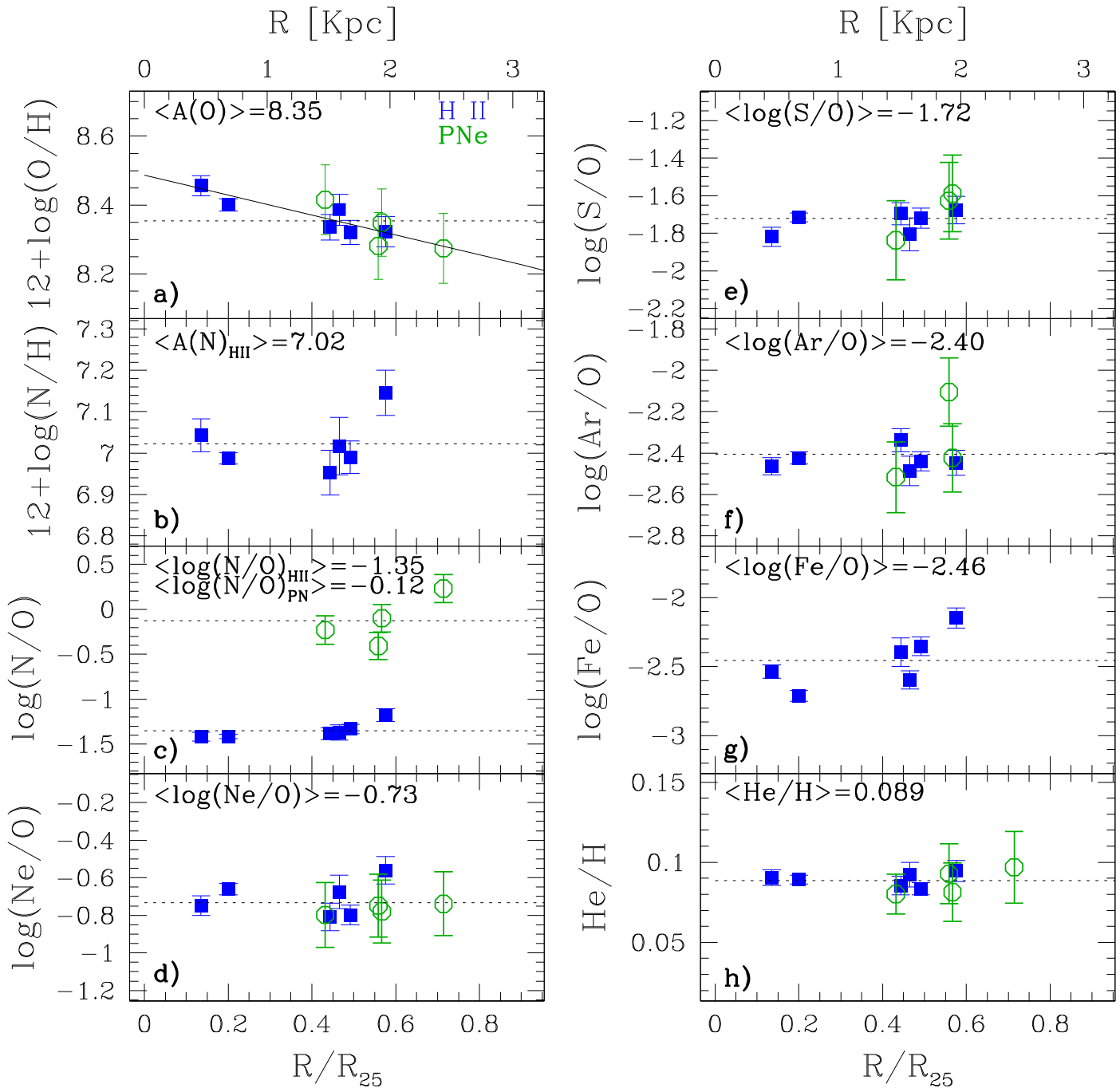

Figure 13. Element abundances and abundance ratios as a function of galactocentric distance R/R_{25}, where $R_{25} = 3.4$ kpc. The linear galactocentric scale in kpc is also indicated on top. Filled and open symbols are for H II regions and PNe, respectively. Within each panel, the label and the dotted horizontal line indicate the average value for the combined H II region and PN data; only in panel (c) are separate log(N/O) mean values for H II regions and PNe provided. In panel (b), in order to better visualize the range of nitrogen variation as a function of radius for H II regions, we do not include PNe, whose N abundance is so high (see Table 6) that the ordinate scale would be too compressed.

data to infer a global relation from a linear least-squares fit:

$$12 + \log(\mathrm{O/H}) = -0.29(\pm 0.06) \times R/R_{25} + 8.49(\pm 0.030). \quad (15)$$

Hence, our gradient[9] is (-0.29 ± 0.08) dex R_{25}^{-1}, in good agreement with the value of (-0.23 ± 0.03) dex R_{25}^{-1} obtained by Pilyugin et al. (2015), once we correct his O/H gradient for the larger distance adopted in his work ($D_{\mathrm{NGC\,4449}} \approx 4.1$ Mpc).

[9] Or (-0.09 ± 0.05) dex R_{Kpc}^{-1} if the actual galactocentric distance R in kpc is considered.

On the other hand, we notice that the central extrapolated oxygen abundance derived by Pilyugin et al. (2015) is $12 + \log(\mathrm{O/H}) = 8.26 \pm 0.01$, more than 0.2 dex lower than ours.

The presence of metallicity gradients in late-type dwarf galaxies has been widely discussed in the literature. For a long time, dIrrs and BCDs have been considered to have nearly constant radial trends, at least within the observational uncertainties (e.g., Kobulnicky & Skillman 1997; Croxall et al. 2009; Haurberg et al. 2013; Lagos & Papaderos 2013). Two possible explanations have been proposed for this behavior: (a) the ejecta from stellar

winds and supernovae are dispersed and mixed across the ISM on short timescales, of the order of $\lesssim 10^7$ yr; (b) freshly synthesized elements remain unmixed with the surrounding ISM and reside in a hot 10^6 K phase or a cold, dusty, molecular phase (Kobulnicky & Skillman 1997). However, detections of negative metallicity gradients from stars and H II regions have been reported in the literature for the dIrr NGC 6822 (Venn et al. 2004; Lee et al. 2006), and spectroscopic studies of individual RGB stars have shown slightly negative gradients in [Fe/H] for the SMC, the LMC, and the dIrr WLM (Leaman et al. 2014, and references therein). Very recently, our study of the BCD NGC 1705 (Annibali et al. 2015) and the study by Pilyugin et al. (2015) showed that negative nebular metallicity gradients are indeed present in late-type dwarf galaxies; our results for NGC 4449 reinforce this scenario. We suspect that these recent studies were able to reveal gradients previously undetected thanks to the high-quality data implied, allowing for much smaller uncertainties on the element abundance determinations.

Figures 13(d)–(f) show a constant trend of the Ne/O, S/O, and Ar/O abundance ratios with galactocentric distance, which, as described in Section 6, is expected because α-elements are all synthesized by massive stars on similar timescales and vary in lockstep. Also the He abundance remains constant with galactocentric distance (Figure 13(h)), in agreement with the absence of any trend of He with oxygen in Figure 12(f). On the other hand, Fe/O decreases with increasing galactocentric distance (Figure 13(g)), which is expected from the presence of an oxygen radial gradient and from the fact that Fe/O decreases with increasing O in Figure 12(e).

Figures 13(b) and (c) show the radial distribution of the N abundance and of the N/O ratio, respectively. The behavior of nitrogen in Figures 13(b) and (c) deserves particular discussion. In fact, despite the existence of a well-defined oxygen metallicity gradient in Figure 13(a), no clear trend of the N abundance with galactocentric distance is observed for H II regions. This behavior is surprising, since we expect that the present ISM in NGC 4449 contains a significant component of secondary N (see, e.g., Vincenzo et al. 2016), implying that an oxygen metallicity gradient should be accompanied by a nitrogen gradient at least as steep (see studies of spiral galaxies, e.g., Diaz & Tosi 1986; Bresolin et al. 2009a; Croxall et al. 2015).

Given the evidence for a conspicuous population of W-R stars in NGC 4449 (Martin & Kennicutt 1997; Bietenholz et al. 2010; Srivastava et al. 2014; Sokal et al. 2015; see also Section 5), local pollution from W-R ejecta enriched in N is an attractive possibility to explain the observed behavior. Although significant amounts of N and C are expected to be injected by W-R stars on theoretical grounds (e.g., Chiosi & Maeder 1986; Dray & Tout 2003; Meynet & Maeder 2005), observational results have been discrepant so far, suggesting either the absence (Kobulnicky & Skillman 1996; Kobulnicky 1999b) or the presence (Kobulnicky et al. 1997; López-Sánchez et al. 2007, 2011; James et al. 2011, 2013) of localized metal enrichment by massive star ejecta. A proposed explanation for these ambiguous results is that an N/O excess is observed only after a recently completed W-R phase, when the W-R features are weak and the ejecta have cooled. In this picture, strong W-R features trace very young regions where the stellar ejecta are still in a hot ($T \approx 10^6$ K) phase and do not show up in optical spectroscopy of H II regions (Tenorio-Tagle 1996; Wofford 2009). This scenario is supported by a study of a large galaxy sample from the Sloan Digital Sky Survey (Brinchmann et al. 2008), where an excess in N/O is found for W-R galaxies with EW(Hβ) < 100 Å (i.e., burst ages $\gtrsim$6 Myr), while W-R and non-WR galaxies do not show a difference in N/O for EW(Hβ) > 100 Å (i.e., burst ages $\lesssim$6 Myr). Indeed, the two regions with strong W-R features in our sample (H II-1 and H II-4) do not exhibit particularly high N/O values, while H II-6, which does not have W-R features but is located in a region of very active SF, presents an N/O excess. Whether there is a correlation in NGC 4449 between the age of the burst and the N abundance for the individual H II regions will be investigated in a forthcoming paper (Sacchi et al. 2017) based on UV LEGUS data (Calzetti et al. 2015).

8. Distinctive Properties of the PN Population

Further insights on the overall evolutionary status of the PNe in NGC 4449 can be attained by considering the full sample of 28 bona fide candidates examined either with spectroscopic or with photometric observations (see Table 7). The statistics is affected by a selection bias, since our PN detection is restrained only to the most active objects with prominent [O III] emission at 5007 Å (for the target to clearly stand out in the V or F502N band frames, compared to B and I imaging). Notice that younger stars do not produce brighter [O III] planetary nebulae; however, at NGC 4449's metallicity and lower, the highest luminosity that a PN can attain increases with increasing oxygen abundance (Dopita et al. 1992; Richer 1993). Therefore, we cannot exclude that our selection criterion has picked up only the most oxygen-rich PNe in NGC 4449.

Within the biased and limited size of our sample, a preliminary, yet useful, estimate of the luminosity-specific PN number density $\alpha = N_{\rm PN}/L_{\rm gal}$ (Jacoby 1980) may be attempted. This parameter directly relates the amount of light in a stellar system to be associated with any observed PN sample, and it closely traces the distinctive evolutionary properties of the underlying stellar population in the parent galaxy. For this task we first require an estimate of NGC 4449 bolometric luminosity, followed by a quantitative assessment of the completeness factor of our PN counts.

The apparent integrated magnitude $V_o^{N4449} = 9.47 \pm 0.3$ and the color $(B-V)_o^{N4449} = 0.36 \pm 0.07$ of NGC 4449 are taken from the corresponding RC3 (de Vaucouleurs et al. 1991) and Gronwall et al. (2004) entries, assuming a Galactic foreground reddening of $E(B-V) = 0.019$ (Schlegel et al. 1998). A match of these figures with the Buzzoni (2005) Im template galaxy model (see Table A7 therein) suggests a bolometric correction in the range $({\rm Bol}-V) = -0.84 \pm 0.02$, from which an absolute value of $M_{\rm bol} = -19.3 \pm 0.3$ and a total bolometric luminosity of $L = (4.0 \pm 1.0) \times 10^9\, L_\odot$ can be obtained, once accounting for the galaxy distance modulus, and assuming for the Sun $M_\odot^{\rm bol} = +4.72$ (Lang 1980).

Our PN completeness level can be estimated by relying on the classical Henize & Westerlund (1963) PN luminosity function (PNLF), in the form of an exponential curve with a sharp truncation designed to accomodate the bright end (see, e.g., Ciardullo et al. 1989; Jacoby & De Marco 2002). An absolute $M_{[\rm O\,III]}$ magnitude (at 10 pc) can be derived for each nebula in our spectroscopic sample, according to the observed [O III] flux of Table 9, corrected for the distance modulus of $(m-M)_0 \sim 27.9$ (Annibali et al. 2008), as $M_{[\rm O\,III]} = -2.5 \log F_{[\rm O\,III]} - 13.74$. These figures can be contrasted with the bright cutoff magnitude ($M^*_{[\rm O\,III]}$) of the Ciardullo et al. (1989)

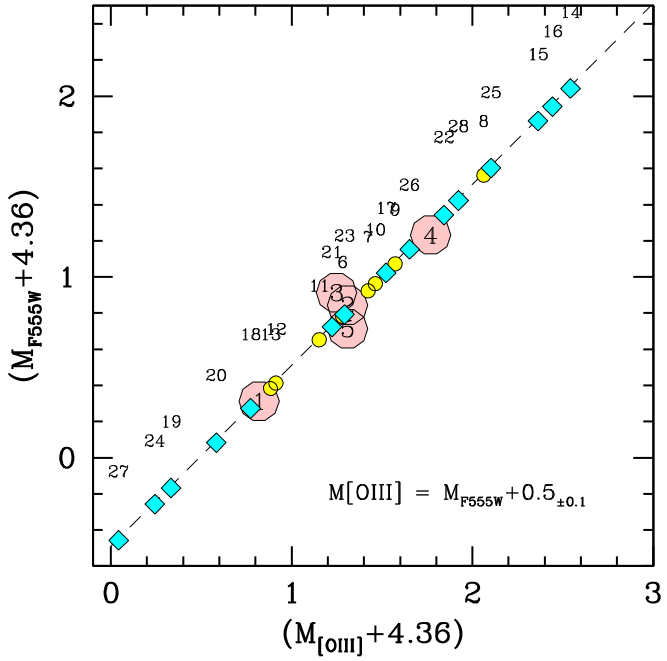

Figure 14. M_{F555W} magnitudes of the spectroscopic PN sample compared to the corresponding $M_{[O\,III]}$ values (big dot markers). All magnitudes have been corrected for the distance modulus and offset by a value of +4.36 mag, corresponding to the PNLF bright cutoff magnitude ($M^*_{[O\,III]}$). A straight relationship is in place with $M_{[O\,III]} - M_{F555W} = 0.5 \pm 0.1$. When applied to the total photometric PN sample (diamonds), this offset allows us to assess the $M_{[O\,III]}$ distribution of the whole sample of 28 PNe, showing that our observations actually probed the bright tail of the NGC 4449 PNLF, down to $(M_{[O\,III]} - M^*_{[O\,III]}) \sim 2.5$ mag. In the plot each nebula is labeled according to its entry ID of Table 7.

PNLF, which, for the NGC 4449 metallicity, can be set at $M^*_{[O\,III]} = -4.36$ (Ciardullo et al. 2002). Our results are summarized in Table 7 and Figure 14.

The figure also provides a mapping between M_{F555W} magnitudes and $M_{[O\,III]}$ magnitudes for the five planetary nebulae with spectroscopy. For this task we relied on the observed m_{F555W} magnitudes, after correcting the Table 7 entries for distance modulus. As expected, the M_{F555W} magnitude of the five spectroscopic nebulae happens to be a quite confident proxy of the corresponding $M_{[O\,III]}$, with $M_{[O\,III]} = M_{F555W} + 0.5 \pm 0.1$ (see Figure 14). When applied to the remaining photometric targets, one can therefore conclude that our observations sample the bright tail of the NGC 4449 PNLF, down to $(M_{[O\,III]} - M^*_{[O\,III]}) \sim 2.5$ mag.

Adopting the standard PNLF, as scaled, for instance, from the M31 (Ciardullo et al. 1989) or LMC observations (Reid & Parker 2010) down to ~8 mag fainter than the bright cutoff limit $M^*_{[O\,III]}$, we obtain a total expected number of 280 ± 53 (Poissonian rms) PNe for our field. A lower value of ~145 ± 27 would be obtained assuming instead the SMC PNLF, as from the deep [O III]5007 observations of Jacoby & De Marco (2002). These values need to be corrected for the fact that we are missing the PNe in the most crowded, central $R/R_{25} \lesssim 0.1$ galaxy regions: adopting the galaxy surface brightness profile of Rich et al. (2012), we estimate a ~40% correction to the PN number, which translates into 392 ± 74 for an assumed Ciardullo et al. (1989) PNLF (or 203 ± 38 PNe assuming the SMC PNLF). We caution that these estimates are highly uncertain because our extrapolation assumes that our sample is proportional to the complete sample from the brightest PN down to ~2.5 mag below the PNLF cutoff; indeed, a robust determination of the PN completeness as a function of magnitude would require artificial star tests performed on the images, which is beyond the scope of this paper.

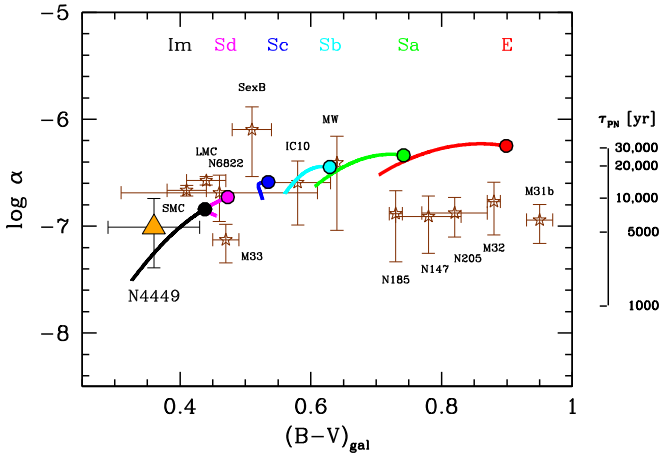

Figure 15. Comprehensive overview of the derived luminosity-specific PN number density α for NGC 4449, compared with Local Group galaxies (stars) as from Buzzoni et al. (2006). Also superposed are the Buzzoni (2005) template galaxy models along the whole morphological sequence from 2 to 15 Gyr, with the latter limit marked by the big filled circles. The Weidemann (2000) empirical scheme is adopted for properly assessing stellar mass loss in the galaxy models. An indicative estimate of the mean representative PN visibility timescale (in years) is sketched on the right scale, as discussed in the text.

With these figures, our estimate of the α parameter leads eventually to

$$\log \alpha = \log\left[\frac{392_{\pm 74}}{4.0_{\pm 0.1}\,10^9}\right] = -7.01^{+0.27}_{-0.38}, \qquad (16)$$

to which, in addition to the Poissonian error from the counts, we attached an uncertainty range that assumes either a 50% fraction of PNe in excess due to a more conservative completeness limit at ~1.5 mag below the bright cutoff or, conversely, a halved reduction of the PN number, as from the Jacoby & De Marco (2002) SMC PNLF.

A comparison with other Local Group galaxies is shown in Figure 15, following Buzzoni et al. (2006). In the plot we also report the theoretical predictions for Buzzoni (2005) template galaxy models, between 2 and 15 Gyr, according to the Weidemann (2000) stellar-mass-loss scheme. The models predict that α decreases in young and/or star-forming galaxies, compared to more quiescent early-type systems as a consequence of a smaller population of PNe embedded in a higher galaxy luminosity per unit mass (i.e., a lower *M/L* ratio). We notice that the luminosity-specific PN number in NGC 4449, as well as the values derived for other late-type systems, agrees quite well with the Buzzoni (2005) models (on the other hand, the models are less successful for the earliest galaxy types).

From a theoretical point of view, the luminosity-specific PN number density easily relates to the reference visibility lifetime (τ_{PN}) of the PN events, being $\alpha = \mathcal{B} \times \tau_{PN}$, with $\mathcal{B}$ the so-called specific evolutionary flux of a stellar population (see Buzzoni et al. 2006, for the theoretical background). The PN visibility lifetime τ_{PN} depends both on the chemical and dynamical properties of the ejected material and on the stellar core evolution during the post-AGB (PAGB) phase. In general, for young and intermediate-age SSPs, the PAGB timescale (τ_{PAGB}) is shorter than the dynamical timescale for the nebula

evaporation, so that the PN lifetime might likely be shorter for more massive, and younger, stellar progenitors. This trend is schematically sketched in Figure 15 relying on the Buzzoni et al. (2006) theoretical framework. According to these models, the typical visibility lifetime for the PNe in NGC 4449 is predicted to be a few thousand years.

9. Conclusions

We presented new deep multiobject spectroscopy with LBT/MODS of H II regions and PNe in the starburst irregular galaxy NGC 4449, at a distance of ≈3.8 Mpc from us. The [O III] λ4363 auroral line was detected in all spectra, allowing for a direct determination of the O^{+2} temperature. For the H II regions, the O^{+} and S^{+2} temperatures were also derived from the [O II] λ7320 + λ7330/λ3726 + λ3729 and [S III] λ6312/λ9069 + λ9532 ratios. Using the "direct" method, we derived the abundance of He, N, O, Ne, Ar, and S for six H II regions and, for the first time, for four PNe in NGC 4449. Iron abundances were also derived for the H II regions, but this element is notoriously highly affected by depletion into dust grains. The combined H II region and PN sample covers a galactocentric distance range of ∼2 kpc, corresponding to ≈70% of the R_{25} isophotal radius. Our main results are as follows:

1. The total H II region + PN sample spans ∼0.2 dex in oxygen abundance, with average 12 + log(O/H) values of 8.37 ± 0.05 and 8.3 ± 0.1 for H II regions and PNe, respectively. The results for the H II regions are consistent, within the errors, with previous literature estimates based on the direct temperature method.
2. We find a well-defined trend of decreasing oxygen abundance with increasing galactocentric distance: 12 + log (O/H) = −0.29(±0.06) × R/R_{25} + 8.49(±0.030), with H II regions and PNe exhibiting similar oxygen abundances at the same galactocentric distance. This result, coupled with our previous finding of a negative metallicity gradient for H II regions in the blue compact dwarf NGC 1705 (Annibali et al. 2015) and with the recent results by Pilyugin et al. (2015), suggests that *metallicity gradients do exist in irregular galaxies*, at odds with what was previously believed (e.g., Kobulnicky & Skillman 1997; Croxall et al. 2009; Haurberg et al. 2013; Lagos & Papaderos 2013).
3. Despite the presence of a negative oxygen gradient, nitrogen does not exhibit any well-defined radial trend. This is unexpected, since an important component of secondary nitrogen should exist in the present-day ISM of NGC 4449. Building on previous literature studies showing evidence for N/O inhomogeneities in W-R galaxies, we suggest that the anomalous nitrogen behavior may be due to local enrichment by the conspicuous W-R population in NGC 4449.
4. The studied PNe exhibit a significant nitrogen enhancement with respect to H II regions (≳1 dex); this behavior is in agreement with previous chemical abundance studies of PNe in galaxies of different morphological types. On the other hand, we also find that the PN helium abundances are similar to those of NGC 4449's H II regions, around He/H ≃ 0.09 (although we caution that our PN He estimates are very uncertain because the detected He I λ5876 line is significantly fainter than two nearby sky lines at λ ∼ 5867 Å and λ ∼ 5890 Å). From the theoretical point of view, we expect both N and He to be enhanced in PNe because they are both synthesized and brought to the stellar surface through dredge-up episodes occurring in the RGB and AGB phases of intermediate-mass stars. We are not aware of any model producing a factor of ∼10 enhancement in N while leaving He unchanged.
5. Our PN oxygen (and α-element, more in general) abundances are, on the other hand, similar to those of H II regions in the galactocentric distance range of overlap. This indicates that NGC 4449's ISM has not been significantly enriched in metals since the progenitors of the PNe were formed (i.e., since ∼100 Myr ago or more). Recently produced α-elements may have been expelled from NGC 4449 by the galactic outflow, or may still reside in a hot phase (see, e.g., Martin et al. 2002, for NGC 1569); also, acquisition of metal-poor gas may have diluted the metals in the ISM.
6. The derived luminosity-specific PN number density ($\alpha = N_{PN}/L_{gal}$) in NGC 4449 agrees quite well with the Buzzoni (2005) template galaxy models that predict the behavior of α as a function of galaxy morphological type and color; according to these models, the α value derived in NGC 4449 translates into a typical visibility lifetime for the PN population of a few thousand years.
7. Two out of the six studied H II regions show broad emission features associated with W-R stars of WN and WC subtypes. From a comparison with population synthesis models, we infer that a W-R population at least 3–4 Myr old must be present in NGC 4449.

F.A. thanks C. Leitherer and E. Skillman for useful discussion, V. Luridiana for support with the Pyneb code, and G. Delgado-Inglada for suggestions related to the use of the new ionization correction factors. We are grateful to the referee, Michael Richer, for his careful reading of the manuscript and for the useful, precise, and constructive comments that helped us to significantly improve the paper. F.A. and this work have been supported financially by PRIN MIUR through grant 2010LY5N2T_006 and by Premiale LBT 2013. D.R. benefited from the International Space Science Institute (ISSI) in Bern, thanks to the funding of the team "The formation and evolution of the galactic halo" (PI: D. Romano). This research was partly supported also by the Munich Institute for Astro- and Particle Physics (MIAPP) of the DFG cluster of excellence "Origin and Structure of the Universe." This work was based on LBT/MODS data. The LBT is an international collaboration among institutions in the United States, Italy, and Germany. LBT Corporation partners are the University of Arizona on behalf of the Arizona Board of Regents; Istituto Nazionale di Astrofisica, Italy; LBT Beteiligungsgesellschaft, Germany, representing the Max-Planck Society, the Leibniz Institute for Astrophysics Potsdam, and Heidelberg University; the Ohio State University; and the Research Corporation, on behalf of the University of Notre Dame, University of Minnesota, and University of Virginia. We acknowledge the support from the LBT-Italian Coordination Facility for the execution of observations, data distribution, and reduction.

Appendix A
H II Regions and PN Spectra

We present the LBT/MODS spectra of H II regions H II-2, H II-3, H II-4, H II-5, and H II-6 in Figures 16–20, respectively, and of planetary nebulae PN-2, PN-3, PN-4, and PN-5 in Figures 21–24, respectively.

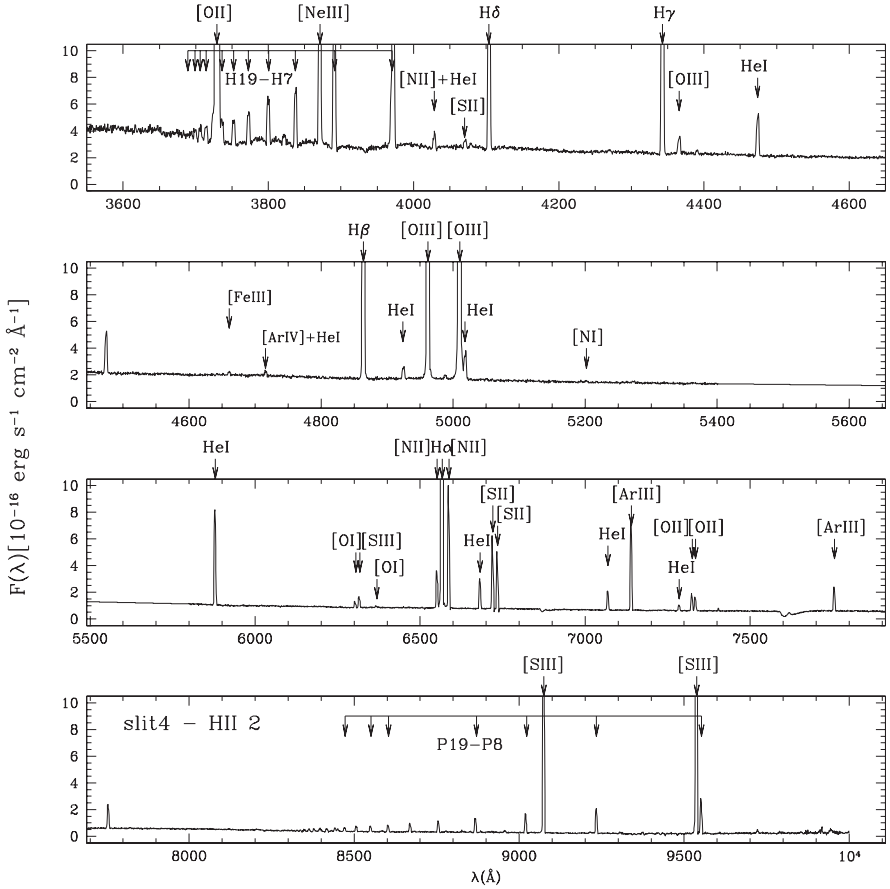

Figure 16. LBT/MODS spectra in the blue and red channels for H II-2 in NGC 4449 with all the identified emission lines indicated. The spectra have been scaled such that the details are evident.

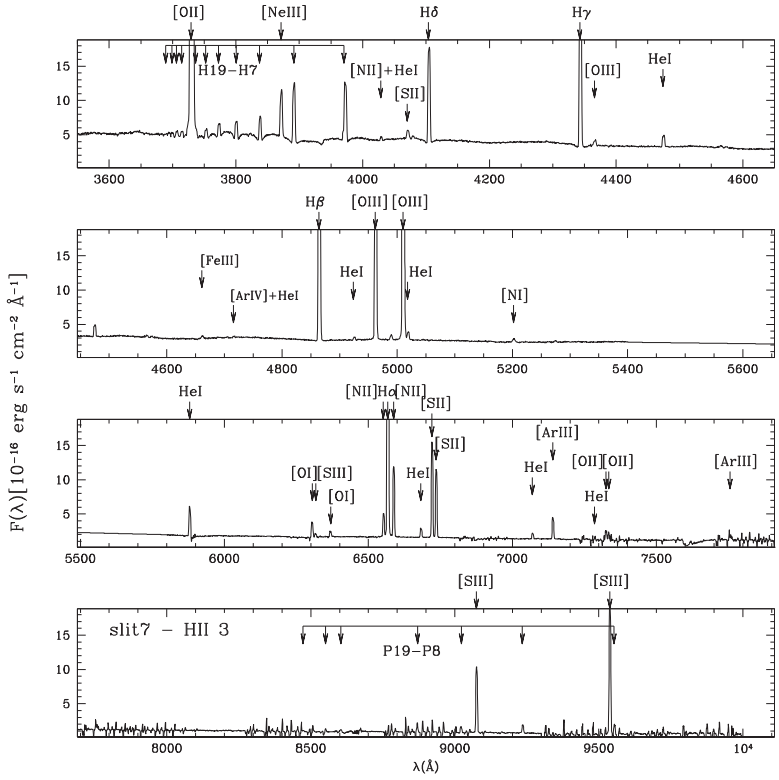

Figure 17. Same as Figure 16, but for H II-3.

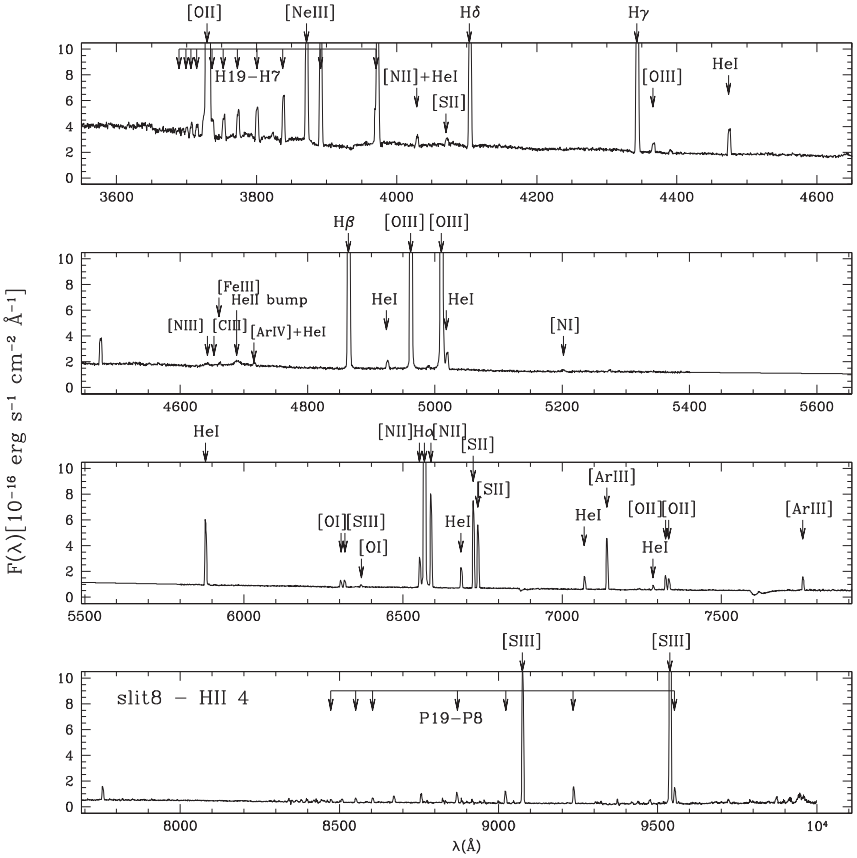

Figure 18. Same as Figure 16, but for H II-4.

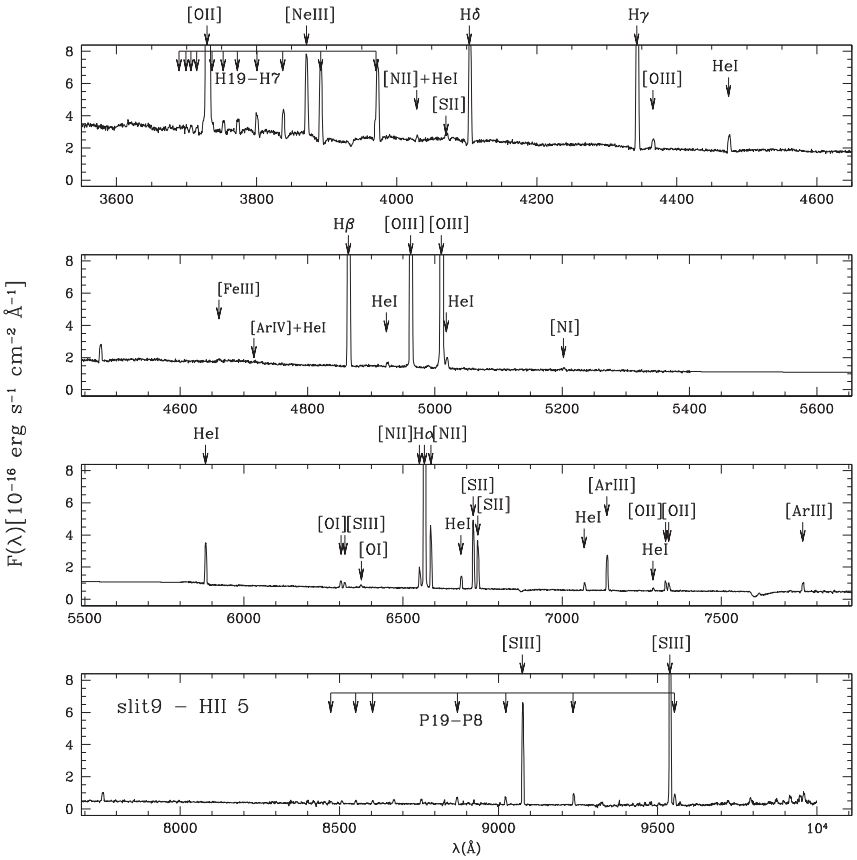

Figure 19. Same as Figure 16, but for H II-5.

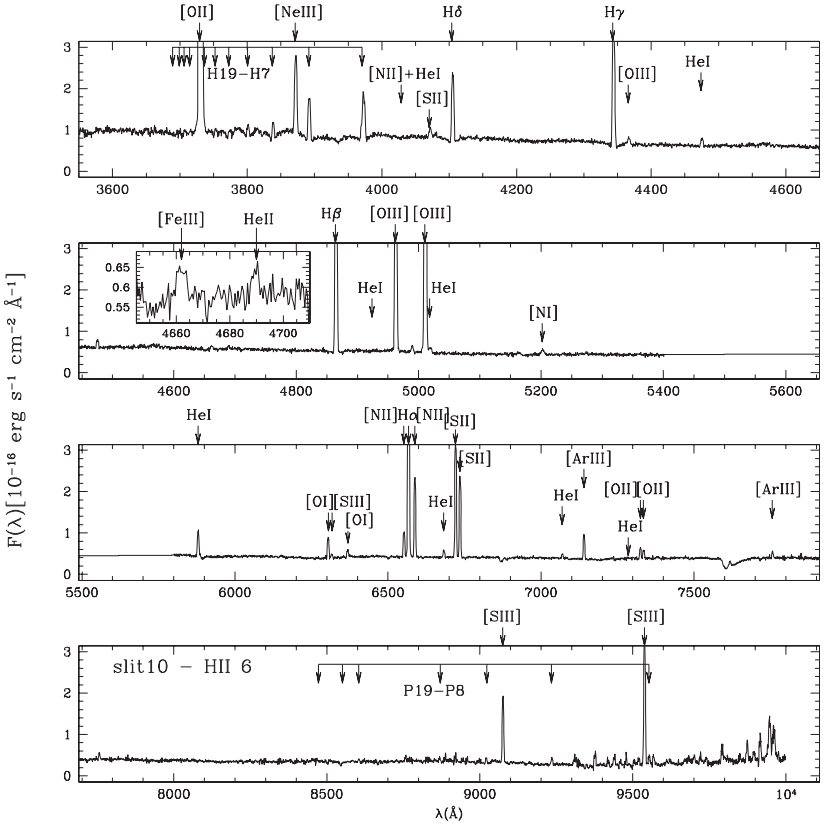

Figure 20. Same as Figure 16, but for H II-6. The small inset provides a zoom-in of the ∼4640–4710 Å wavelength range to highlight the faint [Fe III]λ4658 and He IIλ4686 lines.

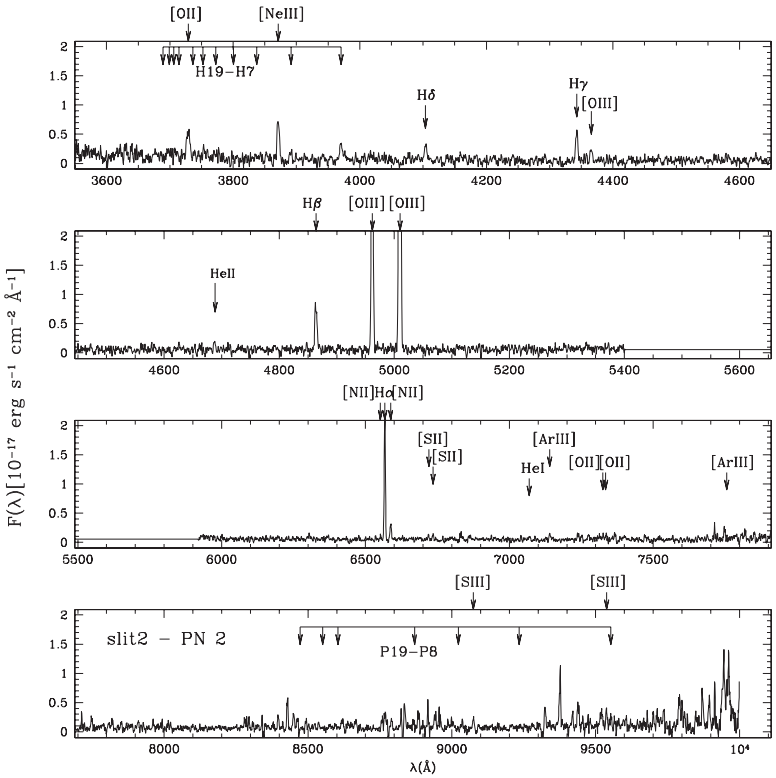

Figure 21. LBT/MODS spectra in the blue and red channels for PN-2 in NGC 4449 with all the identified emission lines indicated. A ∼1 Å boxcar filter smoothing was applied to the spectrum to better highlight the low singal-to-noise ratio features. The spectra have been scaled such that the details are evident.

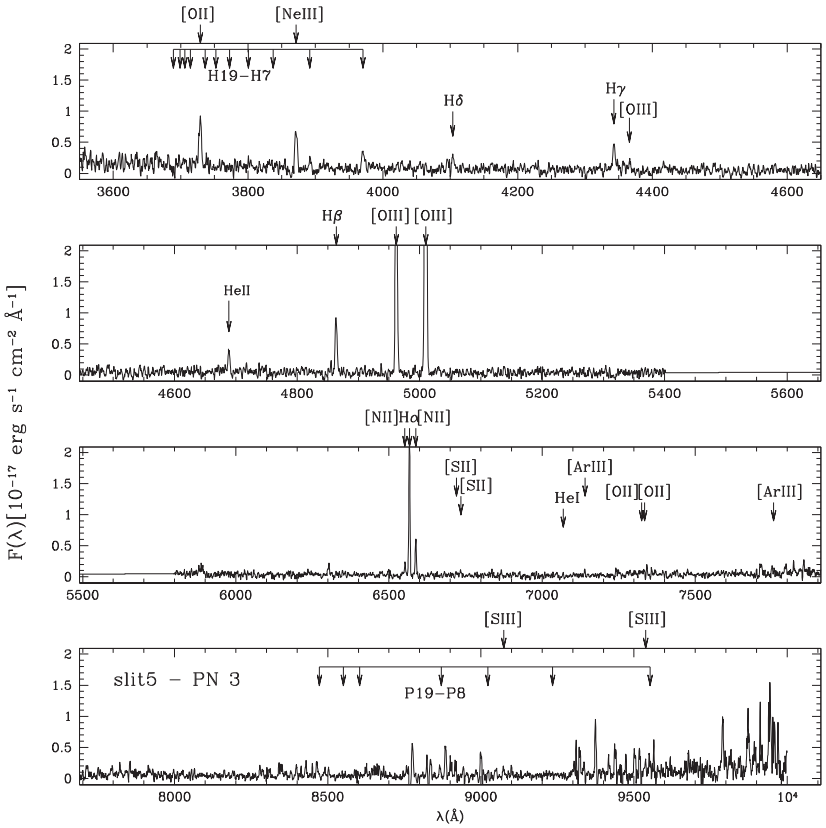

Figure 22. Same as Figure 21, but for PN-3.

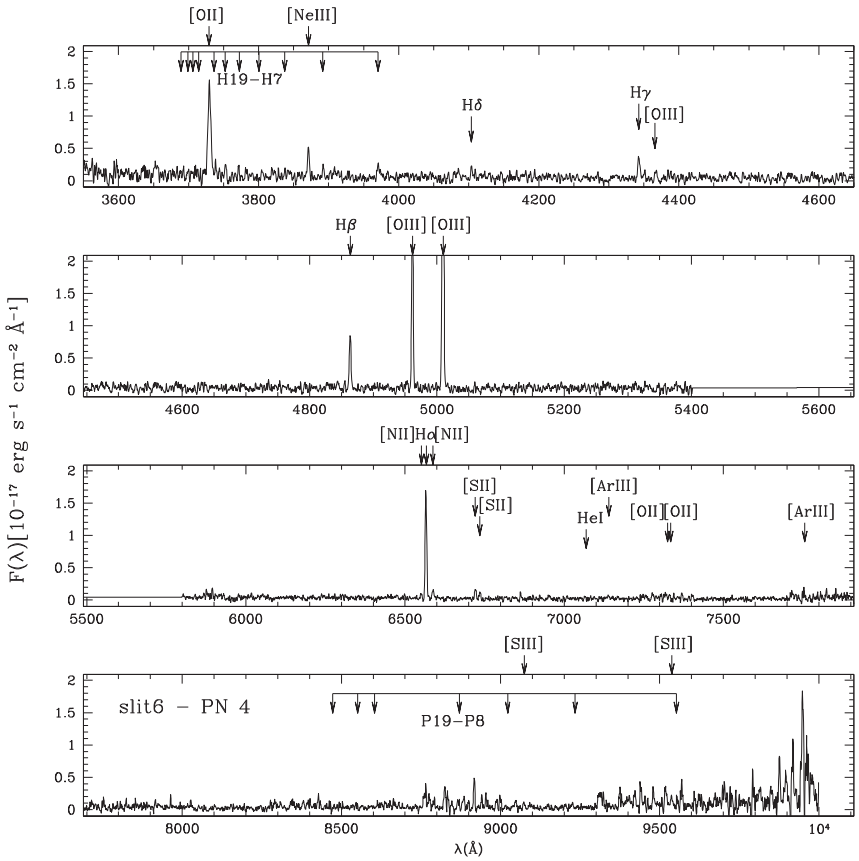

Figure 23. Same as Figure 21, but for PN-4.

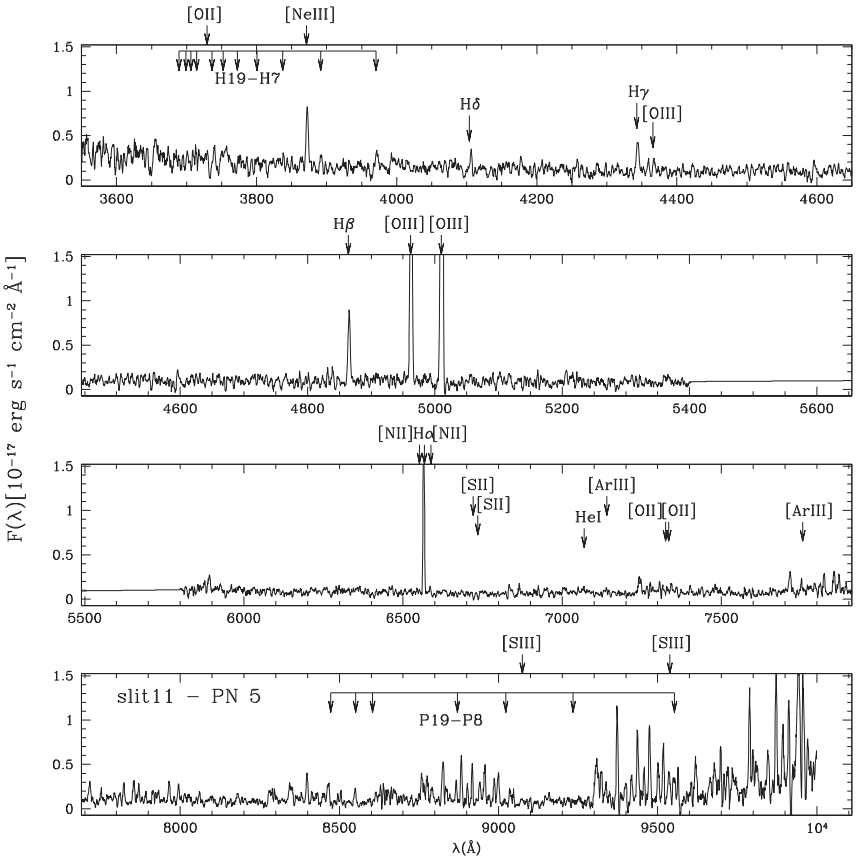

Figure 24. Same as Figure 21, but for PN-5.

Appendix B
"Raw" Emission Line Fluxes

We provide in Tables 8 and 9 the measured emission-line fluxes, with no reddening correction applied, for our studied H II regions and PNe in NGC 4449. The reported flux values were obtained by averaging the results from different measurements, as outlined in Section 3; the associated uncertainties were simply obtained as the standard deviation of the different measurements. Notice that these errors do not account for additional uncertainties due to, e.g., flux calibration.

Table 8
Observed Emission Fluxes for H II Regions in NGC 4449

Line	H II-1	H II-2	H II-3	H II-4	H II-5	H II-6
[O II] λ3727	23.69 ± 0.02	42.85 ± 0.04	75 ± 2	43.62 ± 0.04	24.70 ± 0.03	10.2 ± 0.1
H10 λ3978	1.41 ± 0.01	1.41 ± 0.02	1.19 ± 0.01	1.17 ± 0.01	0.60 ± 0.01	0.13 ± 0.01
He I λ3820	0.210 ± 0.001	0.163 ± 0.001	⋯	0.110 ± 0.001	⋯	⋯
H9+He II λ3835	1.99 ± 0.01	1.907 ± 0.006	1.65 ± 0.01	1.63 ± 0.01	0.837 ± 0.002	0.195 ± 0.001
[Ne III] λ3869	7.22 ± 0.02	5.32 ± 0.01	2.64 ± 0.01	4.08 ± 0.01	1.96 ± 0.01	0.75 ± 0.01
H8+He I λ3889	4.33 ± 0.02	4.96 ± 0.01	3.81 ± 0.01	3.90 ± 0.01	2.19 ± 0.02	0.45 ± 0.01
Hε + He I +[Ne III] λ3970	5.72 ± 0.01	5.44 ± 0.01	4.08 ± 0.01	4.84 ± 0.04	2.56 ± 0.03	0.64 ± 0.01
He I λ4026	0.462 ± 0.006	0.420 ± 0.004	0.18 ± 0.01	0.284 ± 0.001	0.105 ± 0.004	⋯
[S II] λ4068	0.168 ± 0.005	0.184 ± 0.002	0.50 ± 0.01	0.177 ± 0.002	0.143 ± 0.004	0.088 ± 0.001
[S II] λ4076	0.049 ± 0.008	0.095 ± 0.001	0.155 ± 0.002	⋯	⋯	0.034 ± 0.002
Hδ λ4101	6.08 ± 0.01	6.96 ± 0.01	5.96 ± 0.04	6.10 ± 0.03	3.36 ± 0.04	0.69 ± 0.01
Hγ λ4340	10.93 ± 0.01	12.54 ± 0.01	10.46 ± 0.01	9.75 ± 0.01	5.74 ± 0.04	1.25 ± 0.01
[O III] λ4363	0.51 ± 0.02	0.460 ± 0.005	0.289 ± 0.004	0.310 ± 0.003	0.222 ± 0.004	0.059 ± 0.001
He I λ4389	0.137 ± 0.003	0.098 ± 0.003	⋯	0.096 ± 0.002	⋯	⋯
He I λ4471	1.03 ± 0.01	1.15 ± 0.01	0.70 ± 0.01	0.81 ± 0.01	0.39 ± 0.01	0.07 ± 0.01
[N III](WR) λ4640	0.046 ± 0.002	⋯	⋯	0.23 ± 0.01	⋯	⋯
[C III](WR) λ4652	0.028 ± 0.007	⋯	⋯	0.10 ± 0.03	⋯	⋯
[Fe III] λ4658	0.034 ± 0.006	0.078 ± 0.001	0.186 ± 0.004	0.090 ± 0.007	0.060 ± 0.001	0.036 ± 0.004
He II (WR) λ4686	0.89 ± 0.04	⋯	⋯	1.33 ± 0.09	⋯	⋯
He II λ4686	0.10 ± 0.08	⋯	⋯	⋯	⋯	0.022 ± 0.001
[Ar IV]+He I λ4713	0.12 ± 0.01	0.107 ± 0.001	⋯	0.11 ± 0.01	⋯	⋯
[Ar IV] λ4740	0.041 ± 0.003	⋯	⋯	0.064 ± 0.009	⋯	⋯

Table 8
(Continued)

Line	H II-1	H II-2	H II-3	H II-4	H II-5	H II-6
Hβ λ4861	25.02 ± 0.02	29.06 ± 0.01	22.77 ± 0.04	21.76 ± 0.03	12.42 ± 0.01	2.72 ± 0.01
He I λ4922	0.30 ± 0.01	0.35 ± 0.01	0.17 ± 0.01	0.23 ± 0.02	0.10 ± 0.01	⋯
[O III] λ4959	36.190 ± 0.005	38.200 ± 0.008	16.37 ± 0.02	22.95 ± 0.06	14.010 ± 0.005	2.913 ± 0.006
[Fe III] λ4986	0.049 ± 0.004	0.11 ± 0.01	0.268 ± 0.005	0.084 ± 0.001	0.073 ± 0.003	0.054 ± 0.001
[O III] λ5007	106.40 ± 0.01	113.50 ± 0.01	48.22 ± 0.03	67.35 ± 0.02	40.37 ± 0.01	8.45 ± 0.01
He I λ5015	0.624 ± 0.004	0.804 ± 0.003	0.50 ± 0.01	0.52 ± 0.02	0.273 ± 0.002	0.062 ± 0.005
[N I] λ5199	0.054 ± 0.001	0.041 ± 0.001	0.243 ± 0.006	0.059 ± 0.002	0.044 ± 0.001	0.064 ± 0.001
He I λ5876	3.14 ± 0.01	4.04 ± 0.01	2.72 ± 0.04	3.06 ± 0.01	1.57 ± 0.01	0.40 ± 0.01
[O I] λ6302	0.322 ± 0.002	0.231 ± 0.001	⋯	0.283 ± 0.002	0.247 ± 0.002	0.314 ± 0.001
[S III] λ6314	0.307 ± 0.001	0.471 ± 0.001	0.309 ± 0.008	0.321 ± 0.001	0.189 ± 0.001	0.054 ± 0.001
[O I] λ6365	0.102 ± 0.001	0.060 ± 0.004	0.526 ± 0.001	0.102 ± 0.004	0.087 ± 0.002	0.104 ± 0.001
[N II] λ6548	0.80 ± 0.01	1.53 ± 0.02	2.4 ± 0.1	1.42 ± 0.01	0.71 ± 0.01	0.40 ± 0.01
Hα λ6563	79.61 ± 0.01	110.00 ± 0.05	82.6 ± 0.2	82.70 ± 0.01	44.28 ± 0.01	10.55 ± 0.01
[N II] λ6584	2.24 ± 0.03	4.59 ± 0.02	6.8 ± 0.1	4.18 ± 0.01	2.07 ± 0.01	1.22 ± 0.01
He I λ6678	0.965 ± 0.001	1.257 ± 0.004	0.89 ± 0.03	0.984 ± 0.004	0.477 ± 0.001	0.122 ± 0.001
[S II] λ6716	2.29 ± 0.01	2.67 ± 0.01	9.09 ± 0.05	3.93 ± 0.01	2.36 ± 0.01	1.79 ± 0.01
[S II] λ6731	1.67 ± 0.01	2.08 ± 0.01	6.53 ± 0.05	2.90 ± 0.01	1.70 ± 0.01	1.28 ± 0.01
He I λ7065	0.544 ± 0.001	0.802 ± 0.002	0.534 ± 0.001	0.582 ± 0.004	0.278 ± 0.001	0.066 ± 0.001
[Ar III] λ7136	2.388 ± 0.001	3.668 ± 0.005	2.014 ± 0.002	2.223 ± 0.005	1.331 ± 0.001	0.349 ± 0.001
He I λ7281	0.164 ± 0.002	0.235 ± 0.001	⋯	0.167 ± 0.001	0.097 ± 0.001	⋯
[O II] λ7320	0.327 ± 0.002	0.694 ± 0.002	⋯	0.624 ± 0.001	0.353 ± 0.001	0.152 ± 0.001
[O II] λ7330	0.276 ± 0.002	0.592 ± 0.003	⋯	0.508 ± 0.001	0.287 ± 0.001	0.123 ± 0.002
[Ar III] λ7751	0.66 ± 0.01	1.00 ± 0.01	⋯	0.58 ± 0.01	0.38 ± 0.01	0.08 ± 0.01
P10 λ9017	0.582 ± 0.005	0.808 ± 0.006	⋯	0.57 ± 0.02	0.280 ± 0.009	0.055 ± 0.002
[S III] λ9069	6.298 ± 0.002	9.749 ± 0.009	6.36 ± 0.03	6.76 ± 0.02	3.823 ± 0.008	0.965 ± 0.002
P9 λ9229	0.692 ± 0.008	0.989 ± 0.003	0.800 ± 0.004	0.785 ± 0.003	0.426 ± 0.001	⋯
[S III] λ9532	13.200 ± 0.005	24.34 ± 0.04	13.64 ± 0.03	14.67 ± 0.03	8.78 ± 0.02	2.03 ± 0.02
P8 λ9547	0.840 ± 0.009	1.492 ± 0.030	⋯	0.79 ± 0.02	0.44 ± 0.01	⋯
F555W [Vega mag]	18.1	17.6	18.2	18.3	18.5	19.4

Note. The fluxes, in units of 10^{-15} erg s^{-1} cm^{-2} Å^{-1}, were not corrected for reddening. For each line, the reported uncertainty is the standard deviation from different measurements, as described in Section 3.

Table 9
Observed Emission Fluxes for PNe in NGC 4449

Line	PN-1	PN-2	PN-3	PN-4	PN-5
[O II] λ3727	1.28 ± 0.03	2.43 ± 0.03	3.18 ± 0.09	6.92 ± 0.07	⋯
[Ne III] λ3869	3.68 ± 0.03	2.66 ± 0.04	2.51 ± 0.03	1.31 ± 0.02	2.41 ± 0.04
H8+He I λ3889	0.55 ± 0.01	0.71 ± 0.02	0.69 ± 0.02	0.40 ± 0.01	0.49 ± 0.02
Hε + He I +[Ne III] λ3970	1.55 ± 0.02	1.34 ± 0.01	1.37 ± 0.06	0.60 ± 0.01	⋯
Hδ λ4101	1.19 ± 0.02	0.99 ± 0.04	0.71 ± 0.01	⋯	⋯
Hγ λ4340	2.06 ± 0.03	1.91 ± 0.04	1.77 ± 0.09	1.16 ± 0.02	1.41 ± 0.02
[O III] λ4363	0.71 ± 0.01	0.63 ± 0.01	0.62 ± 0.06	0.40 ± 0.02	0.53 ± 0.01
He II λ4686	<0.15	0.55 ± 0.03	1.37 ± 0.02	<0.15	<0.2
Hβ λ4861	5.21 ± 0.03	3.36 ± 0.03	3.50 ± 0.07	2.44 ± 0.04	3.10 ± 0.02
[O III] λ4959	20.29 ± 0.02	13.84 ± 0.02	13.9 ± 0.1	8.25 ± 0.01	13.63 ± 0.01
[O III] λ5007	59.06 ± 0.05	40.30 ± 0.03	40.15 ± 0.07	24.2 ± 0.2	38.08 ± 0.02
He I λ5876	0.59 ± 0.01	0.38 ± 0.03	0.24 ± 0.01	0.34 ± 0.02	0.47 ± 0.03
[N II] λ6548	0.54 ± 0.02	0.34 ± 0.02	0.83 ± 0.01	0.40 ± 0.01	0.16 ± 0.02
Hα λ6563	14.50 ± 0.03	10.12 ± 0.02	9.19 ± 0.01	9.96 ± 0.02	9.77 ± 0.02
[N II] λ6584	1.31 ± 0.02	1.30 ± 0.01	2.49 ± 0.01	0.84 ± 0.01	0.37 ± 0.01
[S II] λ6716	0.54 ± 0.03	0.41 ± 0.02	0.30 ± 0.01	0.98 ± 0.01	⋯
[S II] λ6731	0.55 ± 0.04	0.37 ± 0.02	0.38 ± 0.01	0.66 ± 0.01	⋯
He I λ7065	0.74 ± 0.03	⋯	⋯	⋯	0.25 ± 0.01
[Ar III] λ7136	0.40 ± 0.01	0.63 ± 0.02	0.30 ± 0.01	⋯	⋯
[S III] λ9069	0.92 ± 0.02	0.90 ± 0.01	0.65 ± 0.03	⋯	⋯
[S III] λ9532	1.71 ± 0.08	⋯	⋯	⋯	⋯
F555W [Vega mag]	23.9	24.4	24.5	24.8	24.3

Note. The fluxes, in units of 10^{-17} erg s^{-1} cm^{-2} Å^{-1}, were not corrected for reddening. For each line, the reported uncertainty is the standard deviation from different measurements, as described in Section 3.

Appendix C
PN Chemical Abundances with New Ionization Correction Factors

Recently, Delgado-Inglada et al. (2014, hereafter DMS14) presented new ICFs for PNe using a large grid of photoionization models covering a wide range of physical parameters. Analytical expressions for the uncertainties associated with the new ICFs are also provided. We performed a comparison of the ICFs from Kingsburgh & Barlow (1994) (KB94), used in Section 4.2 of this paper, with the new DMS14 recipes and evaluated the effect on the derived PN chemical abundances. Figure 25 shows the difference in abundance due to the use of the new ICFs by DMS14 compared to the old ICFs by KB94.

For helium, DMS14 suggest to calculate the He/H total abundance simply by adding He^{+}/H^{+} and He^{++}/H^{+}, i.e., neglecting any correction for neutral helium. This corresponds to the same approach that we adopted in Section 4.2; therefore, no comparison needs to be made for He.

For oxygen, DMS14 propose

$$O = (O^{+} + O^{++}) \times ICF(O^{+} + O^{++}), \quad (17)$$

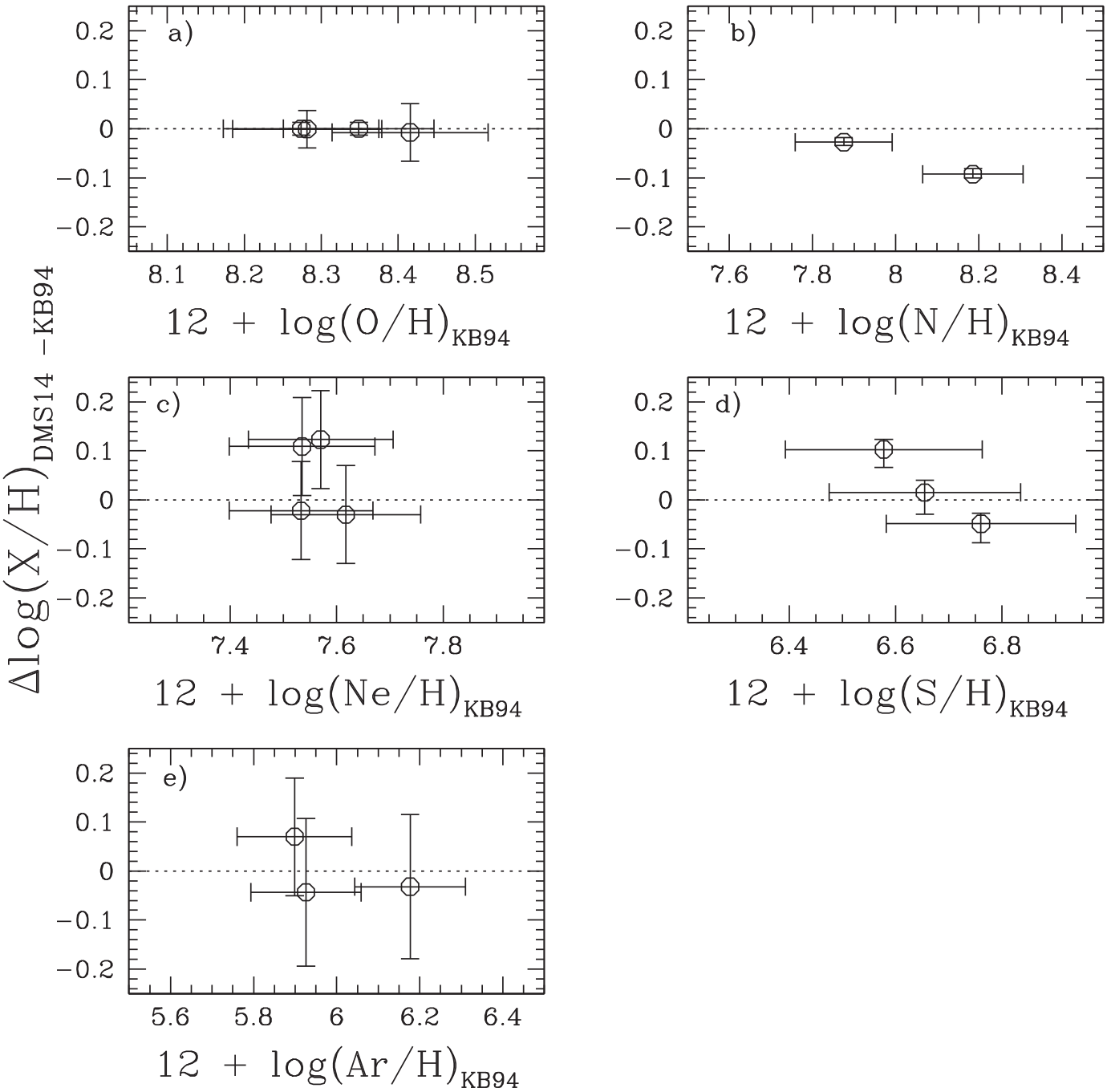

Figure 25. Abundance difference due to the use of the new ICFs by DMS14 compared to the old ICFs by KB94, used in Section 4.2 of this paper (see the text for details).

where

$$\log \mathrm{ICF}(\mathrm{O}^{+}+\mathrm{O}^{++})=\frac{0.08v+0.006v^{2}}{0.34-0.27v} \quad (18)$$

and

$$v=\frac{\mathrm{He}^{++}}{(\mathrm{He}^{+}+\mathrm{He}^{++})};\qquad w=\frac{\mathrm{O}^{++}}{(\mathrm{O}^{+}+\mathrm{O}^{++})}. \quad (19)$$

Equation (18) is valid for $v \leqslant 0.95$ and thus applies to all our four PNe. Panel (a) of Figure 25 shows that the difference in O abundance due to the use of the new ICFs is very small (a few percent in dex) and largely below the errors associated with the derived $12+\log(\mathrm{O/H})$ values.

For nitrogen, DMS14 propose the following formulae valid only until $w=0.95$:

$$\frac{\mathrm{N}}{\mathrm{O}}=\frac{\mathrm{N}^{+}}{\mathrm{O}^{+}}\times \mathrm{ICF}(\mathrm{N}^{+}/\mathrm{O}^{+}), \quad (20)$$

where

$$\log \mathrm{ICF}(\mathrm{N}^{+}/\mathrm{O}^{+})=-0.16w(1+\log v) \quad (21)$$

when He II lines are detected and

$$\log \mathrm{ICF}(\mathrm{N}^{+}/\mathrm{O}^{+})=0.64w \quad (22)$$

when He II lines are not detected. However, Equation (22) may work fine for matter-bounded nebulae but not for radiation-bounded models, and therefore the recommendation is to use the usual $\mathrm{N/O}=\mathrm{N}^{+}/\mathrm{O}^{+}$ expression until the issue is further explored (G. Delgado-Inglada 2017, private communication). In our sample, the condition $w \leqslant 0.95$ is only satisfied by PN-2 and PN-3, with observed He II lines, and therefore we used Equation (21) to compute the new abundances. Panel (b) of Figure 25 shows that the new N abundances tend to be lower than the previous ones; however, the difference is within $\sim$0.1 dex, i.e., comparable to the uncertainty associated with the $12+\log(\mathrm{N/H})$ values.

For neon, the abundance is

$$\frac{\mathrm{Ne}}{\mathrm{O}}=\frac{\mathrm{Ne}^{++}}{\mathrm{O}^{++}}\times \mathrm{ICF}(\mathrm{Ne}^{++}/\mathrm{O}^{++}), \quad (23)$$

where

$$\mathrm{ICF}(\mathrm{Ne}^{++}/\mathrm{O}^{++})=w+\left(\frac{0.014}{v'}+2v'^{2.7}\right)^{3}\times(0.7+0.2w-0.8w^{2}); \quad (24)$$

$v'=0.01$ if no He II lines are detected (PN-1 and PN-5), and $v'=v$ if $v \geqslant 0.015$ (PN-2 and PN-3). Panel (c) of Figure 25 shows that the difference in Ne abundance is within $\sim$0.1 dex, smaller than the errors for the $12+\log(\mathrm{Ne/H})$ values; notice also the large uncertainties associated with the ICFs for Ne.

For sulfur, we measure both S^{+} and S^{++} in PN-1, PN-2, and PN-3; therefore, DMS14 provides

$$\frac{\mathrm{S}}{\mathrm{O}}=\frac{\mathrm{S}^{+}+\mathrm{S}^{++}}{\mathrm{O}^{+}}\times \mathrm{ICF}((\mathrm{S}^{+}+\mathrm{S}^{++})/\mathrm{O}^{+}), \quad (25)$$

where

$$\log \mathrm{ICF}((\mathrm{S}^{+}+\mathrm{S}^{++})/\mathrm{O}^{+})=\frac{-0.02-0.03w-2.31w^{2}+2.19w^{3}}{0.69+2.09w-2.69w^{2}} \quad (26)$$

if $I(\mathrm{He\ II})/I(\mathrm{H}\beta) \geqslant 0.02$ and

$$\mathrm{ICF}((\mathrm{S}^{+}+\mathrm{S}^{++})/\mathrm{O}^{+})=1 \quad (27)$$

in all the other cases. We measure $I(\mathrm{He\ II})/I(\mathrm{H}\beta)\sim 0.2$ and $\sim$0.4 in PN-2 and PN-3, respectively, while for PN-1 we have only an upper limit of $I(\mathrm{He\ II})/I(\mathrm{H}\beta)<0.03$ from Table 9; therefore, Equation (26) is applied to all three PNe. Panel (d) of Figure 25 shows no systematic trend of the new S abundances with respect to the old ones; the differences are within $\sim$0.1 dex, i.e., lower than the errors associated with the $12+\log(\mathrm{S/H})$ values.

Finally, the DMS14 recipe for argon is

$$\mathrm{Ar}=\mathrm{Ar}^{++}\times\frac{\mathrm{O}}{\mathrm{O}^{+}+\mathrm{O}^{++}}\times \mathrm{ICF}(\mathrm{Ar}^{++}/(\mathrm{O}^{+}+\mathrm{O}^{++}), \quad (28)$$

where, for $w>0.5$ (i.e., PN-1, PN-2, PN-3, PN-5),

$$\log \mathrm{ICF}(\mathrm{Ar}^{++}/(\mathrm{O}^{+}+\mathrm{O}^{++})=\frac{0.03w}{0.4-0.3w}-0.05. \quad (29)$$

Panel (e) of Figure 25 shows again differences in the Ar abundances within $\sim$0.1 dex, smaller than the uncertainty in the computed $12+\log(\mathrm{Ar/H})$ values.

References

Abel, N. P., Ferland, G. J., Shaw, G., & van Hoof, P. A. M. 2005, ApJS, 161, 65
Aggarwal, K. M., & Keenan, F. P. 1999, ApJS, 123, 311
Annibali, F., Aloisi, A., Mack, J., et al. 2008, AJ, 135, 1900
Annibali, F., Tosi, M., Aloisi, A., & van der Marel, R. P. 2011, AJ, 142, 129
Annibali, F., Tosi, M., Aloisi, A., van der Marel, R. P., & Martinez-Delgado, D. 2012, ApJL, 745, L1
Annibali, F., Tosi, M., Pasquali, A., et al. 2015, AJ, 150, 143
Berg, D. A., Skillman, E. D., Croxall, K. V., et al. 2015, ApJ, 806, 16
Berg, D. A., Skillman, E. D., Marble, A. R., et al. 2012, ApJ, 754, 98
Bietenholz, M. F., Bartel, N., Milisavljevic, D., et al. 2010, MNRAS, 409, 1594
Bomans, D. J., & Weis, K. 2014, AN, 335, 99
Bresolin, F. 2011, ApJ, 730, 129
Bresolin, F., Gieren, W., Kudritzki, R.-P., et al. 2009a, ApJ, 700, 309
Bresolin, F., Ryan-Weber, E., Kennicutt, R. C., & Goddard, Q. 2009b, ApJ, 695, 580
Bresolin, F., Schaerer, D., González Delgado, R. M., & Stasińska, G. 2005, A&A, 441, 981
Bresolin, F., Stasińska, G., Vílchez, J. M., Simon, J. D., & Rosolowsky, E. 2010, MNRAS, 404, 1679
Brinchmann, J., Kunth, D., & Durret, F. 2008, A&A, 485, 657
Buzzoni, A. 2005, MNRAS, 361, 725
Buzzoni, A., Arnaboldi, M., & Corradi, R. L. M. 2006, MNRAS, 368, 877
Calzetti, D., Kinney, A. L., & Storchi-Bergmann, T. 1996, ApJ, 458, 132
Calzetti, D., Lee, J. C., Sabbi, E., et al. 2015, AJ, 149, 51
Cardelli, J. A., Clayton, G. C., & Mathis, J. S. 1989, ApJ, 345, 245
Chavez, M., Bertone, E., Morales-Hernandez, J., & Bressan, A. 2009, ApJ, 700, 694
Chiosi, C., & Maeder, A. 1986, ARA&A, 24, 329
Ciardullo, R., Feldmeier, J. J., Jacoby, G. H., et al. 2002, ApJ, 577, 31
Ciardullo, R., Jacoby, G. H., Ford, H. C., & Neill, J. D. 1989, ApJ, 339, 53
Clegg, R. E. S. 1987, MNRAS, 229, 31P

Corradi, R. L. M., & Schwarz, H. E. 1995, A&A, 293, 871
Croxall, K. V., Pogge, R. W., Berg, D. A., Skillman, E. D., & Moustakas, J. 2015, ApJ, 808, 42
Croxall, K. V., Pogge, R. W., Berg, D. A., Skillman, E. D., & Moustakas, J. 2016, ApJ, 830, 4
Croxall, K. V., van Zee, L., Lee, H., et al. 2009, ApJ, 705, 723
Dalcanton, J. J., Williams, B. F., Lang, D., et al. 2012, ApJS, 200, 18
Dalcanton, J. J., Williams, B. F., Seth, A. C., et al. 2009, ApJS, 183, 67
De Robertis, M. M., Dufour, R. J., & Hunt, R. W. 1987, JRASC, 81, 195
de Vaucouleurs, G., de Vaucouleurs, A., Corwin, H. G., Jr., et al. 1991, Third Reference Catalog of Bright Galaxies (Heidelberg: Springer)
Dekel, A., Birnboim, Y., Engel, G., et al. 2009, Natur, 457, 451
Delgado-Inglada, G., Morisset, C., & Stasińska, G. 2014, MNRAS, 440, 536
Delgado-Inglada, G., Rodríguez, M., García-Rojas, J., Peña, M., & Ruiz, M. T. 2011, RMxAC, 40, 165
Della Ceca, R., Griffiths, R. E., & Heckman, T. M. 1997, ApJ, 485, 581
Diaz, A. I., & Tosi, M. 1986, A&A, 158, 60
Dopita, M. A., Jacoby, G. H., & Vassiliadis, E. 1992, ApJ, 389, 27
Dray, L. M., & Tout, C. A. 2003, MNRAS, 341, 299
Dray, L. M., Tout, C. A., Karakas, A. I., & Lattanzio, J. C. 2003, MNRAS, 338, 973
Eldridge, J. J., Izzard, R. G., & Tout, C. A. 2008, MNRAS, 384, 1109
Filippenko, A. V. 1982, PASP, 94, 715
Galavis, M. E., Mendoza, C., & Zeippen, C. J. 1995, A&AS, 111, 347
Galavis, M. E., Mendoza, C., & Zeippen, C. J. 1997, A&AS, 123, 159
García-Rojas, J., Peña, M., Flores-Durán, S., & Hernández-Martínez, L. 2016, A&A, 586, A59
Garnett, D. R. 1992, AJ, 103, 1330
Gronwall, C., Salzer, J. J., Sarajedini, V. L., et al. 2004, AJ, 127, 1943
Guseva, N. G., Izotov, Y. I., Stasińska, G., et al. 2011, A&A, 529, AA149
Hägele, G. F., Pérez-Montero, E., Díaz, Á I., Terlevich, E., & Terlevich, R. 2006, MNRAS, 372, 293
Hanuschik, R. W. 2003, A&A, 407, 1157
Haurberg, N. C., Rosenberg, J., & Salzer, J. J. 2013, ApJ, 765, 66
Henize, K. G., & Westerlund, B. E. 1963, ApJ, 137, 747
Hunter, D. A., Wilcots, E. M., van Woerden, H., Gallagher, J. S., & Kohle, S. 1998, ApJL, 495, L47
Idiart, T. P., Maciel, W. J., & Costa, R. D. D. 2007, A&A, 472, 101
Izotov, Y. I., Stasińska, G., & Guseva, N. G. 2013, A&A, 558, A57
Izotov, Y. I., Stasińska, G., Meynet, G., Guseva, N. G., & Thuan, T. X. 2006, A&A, 448, 955
Izotov, Y. I., Thuan, T. X., & Stasińska, G. 2007, ApJ, 662, 15
Jacoby, G. 1980, ApJ, 42, 1
Jacoby, G. H., & De Marco, O. 2002, AJ, 123, 269
James, B. L., Tsamis, Y. G., Barlow, M. J., et al. 2011, EAS, 48, 109
James, B. L., Tsamis, Y. G., Walsh, J. R., Barlow, M. J., & Westmoquette, M. S. 2013, MNRAS, 430, 2097
Kaler, J. B. 1986, ApJ, 308, 322
Karakas, A., & Lattanzio, J. C. 2007, PASA, 24, 103
Karakas, A. I. 2010, MNRAS, 403, 1413
Kaufman, V., & Sugar, J. 1986, JPCRD, 15, 321
Kennicutt, R. C., Jr., Bresolin, F., & Garnett, D. R. 2003, ApJ, 591, 801
Kingsburgh, R. L., & Barlow, M. J. 1994, MNRAS, 271, 257
Kobulnicky, H. A. 1999b, in Proc. IAU Symp. 193, Chemical Enrichment from Massive Stars in Starbursts, ed. K. A. van der Hucht, G. Koenigsberger, & P. R. J. Eenens (San Francisco, CA: ASP), 670
Kobulnicky, H. A., & Skillman, E. D. 1996, ApJ, 471, 211
Kobulnicky, H. A., & Skillman, E. D. 1997, ApJ, 489, 636
Kobulnicky, H. A., Skillman, E. D., Roy, J.-R., Walsh, J. R., & Rosa, M. R. 1997, ApJ, 477, 679
Lagos, P., & Papaderos, P. 2013, AdAst, 2013, 20
Lang, K. R. 1980, Astrophysical Formulae (Berlin: Springer), 563
Leaman, R., Venn, K., Brooks, A., et al. 2014, MmSAI, 85, 504
Lee, H., Skillman, E. D., & Venn, K. A. 2006, ApJ, 642, 813
Leitherer, C., Ekström, S., Meynet, G., et al. 2014, ApJS, 212, 14
Leitherer, C., Lee, J., & Levesque, E. 2017, in Proc. IAU Symp. 329, The Lives and Death-throes of Massive Stars, in press
Lelli, F., Verheijen, M., & Fraternali, F. 2014, MNRAS, 445, 1694
López-Sánchez, Á R., Esteban, C., García-Rojas, J., Peimbert, M., & Rodríguez, M. 2007, ApJ, 656, 168
López-Sánchez, Á R., Mesa-Delgado, A., López-Martín, L., & Esteban, C. 2011, MNRAS, 411, 2076
Luridiana, V., Morisset, C., & Shaw, R. A. 2015, A&A, 573, A42
Maeder, A. 1991, A&A, 242, 93
Maeder, A., & Conti, P. S. 1994, ARA&A, 32, 227
Magrini, L., & Gonçalves, D. R. 2009, MNRAS, 398, 280
Magrini, L., Leisy, P., Corradi, R. L. M., et al. 2005, A&A, 443, 115
Marigo, P. 2001, A&A, 370, 194
Marigo, P., Girardi, L., Bressan, A., et al. 2008, A&A, 482, 883
Martin, C. L., & Kennicutt, R. C., Jr. 1997, ApJ, 483, 698
Martin, C. L., Kobulnicky, H. A., & Heckman, T. M. 2002, ApJ, 574, 663
Martínez-Delgado, D., Romanowsky, A. J., Gabany, R. J., et al. 2012, ApJL, 748, L24
McLaughlin, B. M., & Bell, K. L. 2000, JPhB, 33, 597
McQuinn, K. B. W., Skillman, E. D., Cannon, J. M., et al. 2010, ApJ, 724, 49
Mendoza, C. 1983, in IAU Symp. 103, Planetary Nebulae (Dordrecht: Reidel), 143
Meynet, G., & Maeder, A. 2002, A&A, 381, L25
Meynet, G., & Maeder, A. 2005, A&A, 429, 581
Meynet, G., Maeder, A., Schaller, G., Schaerer, D., & Charbonnel, C. 1994, A&AS, 103, 97
Monelli, M., Gallart, C., Hidalgo, S. L., et al. 2010a, ApJ, 722, 1864
Monelli, M., Hidalgo, S. L., Stetson, P. B., et al. 2010b, ApJ, 720, 1225
Niedzielski, A., & Skorzynski, W. 2002, AcA, 52, 81
Peña, M., Richer, M. G., & Stasińska, G. 2007, A&A, 466, 75
Pilyugin, L. S., Grebel, E. K., & Zinchenko, I. A. 2015, arXiv:1505.00337
Podobedova, L. I., Kelleher, D. E., & Wiese, W. L. 2009, JPCRD, 38, 2
Porter, R. L., Ferland, G. J., Storey, P. J., & Detisch, M. J. 2012, MNRAS, 425, L28
Porter, R. L., Ferland, G. J., Storey, P. J., & Detisch, M. J. 2013, MNRAS, 433, L89
Pradhan, A. K., Montenegro, M., Nahar, S. N., & Eissner, W. 2006, MNRAS, 366, L6
Reid, W. A., & Parker, Q. A. 2010, MNRAS, 405, 1349
Renzini, A., & Voli, M. 1981, A&A, 94, 175
Rich, R. M., Collins, M. L. M., Black, C. M., et al. 2012, Natur, 482, 192
Richer, M. G. 1993, ApJ, 415, 240
Richer, M. G., & McCall, M. L. 2007, ApJ, 658, 328
Richer, M. G., & McCall, M. L. 2008, ApJ, 684, 1190
Romano, D., Karakas, A. I., Tosi, M., & Matteucci, F. 2010, A&A, 522, A32
Romano, D., Tosi, M., & Matteucci, F. 2006, MNRAS, 365, 759
Sacchi, E., Cignoni, M., Aloisi, A., et al. 2017, ApJ, submitted
Schaerer, D., & Maeder, A. 1992, A&A, 263, 129
Schaller, G., Schaerer, D., Meynet, G., & Maeder, A. 1992, A&AS, 96, 269
Schlegel, D. J., Finkbeiner, D. P., & Davis, M. 1998, ApJ, 500, 525
Shaw, R. A., & Dufour, R. J. 1994, in ASP. Conf. Ser. 61, Astronomical Data Analysis Software and Systems III, ed. D. R. Crabtree, R. J. Hanisch, & J. Barnes (San Francisco, CA: ASP), 327
Skillman, E. D., Kennicutt, R. C., & Hodge, P. W. 1989, ApJ, 347, 875
Smith, J. D. T., Armus, L., Dale, D. A., et al. 2007, PASP, 119, 1133
Smith, L. J., Crowther, P. A., Calzetti, D., & Sidoli, F. 2016, ApJ, 823, 38
Sokal, K. R., Johnson, K. E., Indebetouw, R., & Reines, A. E. 2015, AJ, 149, 115
Srivastava, S., Kantharia, N. G., Basu, A., Srivastava, D. C., & Ananthakrishnan, S. 2014, MNRAS, 443, 860
Stanghellini, L., Guerrero, M. A., Cunha, K., Manchado, A., & Villaver, E. 2006, ApJ, 651, 898
Stasińska, G., Peña, M., Bresolin, F., & Tsamis, Y. G. 2013, A&A, 552 A12
Storey, P. J., & Hummer, D. G. 1995, MNRAS, 272, 41
Storey, P. J., & Zeippen, C. J. 2000, MNRAS, 312, 813
Summers, L. K., Stevens, I. R., Strickland, D. K., & Heckman, T. M. 2003, MNRAS, 342, 690
Talent, D. L. 1980, BAAS, 12, 866
Tayal, S. S. 2007, ApJS, 171, 331
Tayal, S. S. 2011, ApJS, 195, 12
Tayal, S. S., & Gupta, G. P. 1999, ApJ, 526, 544
Tayal, S. S., & Zatsarinny, O. 2010, ApJS, 188, 32
Tenorio-Tagle, G. 1996, AJ, 111, 1641
Tinsley, B. M. 1980, FCPh, 5, 287
Tolstoy, E., Hill, V., & Tosi, M. 2009, ARA&A, 47, 371
Torres-Peimbert, S., & Peimbert, M. 1997, in Proc. 180th IAU Symp., Planetary Nebulae, ed. H. J. Habing & H. J. G. L. M. Lamers (Dordrecht: Kluwer) 175
Vanbeveren, D., Van Bever, J., & Belkus, H. 2007, ApJL, 662, L107
Venn, K. A., Tolstoy, E., Kaufer, A., & Kudritzki, R. P. 2004, in Origin and Evolution of the Elements, ed. A. McWilliam & M. Rauch, 58

Ventura, P., Di Criscienzo, M., Carini, R., & D'Antona, F. 2013, MNRAS, 431, 3642
Vincenzo, F., Belfiore, F., Maiolino, R., Matteucci, F., & Ventura, P. 2016, MNRAS, 458, 3466
Wang, W., & Liu, X.-W. 2007, MNRAS, 381, 669
Weidemann, V. 2000, A&A, 363, 647
Weisz, D. R., Dalcanton, J. J., Williams, B. F., et al. 2011, ApJ, 739, 5
Weisz, D. R., Dolphin, A. E., Skillman, E. D., et al. 2014, ApJ, 789 147
Wiese, W. L., Fuhr, J. R., & Deters, T. M. (ed.) 1996, Atomic Transition Probabilities of Carbon, Nitrogen, and Oxygen: A Critical Data Compilation (Melville, NY: AIP)
Wofford, A. 2009, MNRAS, 395, 1043
Zeippen, C. J. 1982, MNRAS, 198, 111